Theoretical Studies of Reduction Reactions of Nitrogen Oxides Mediated by Copper Complexes

亀谷, 陽平

主論文

Theoretical Studies of Reduction Reactions of Nitrogen Oxides Mediated by Copper Complexes

銅錯体による窒素酸化物還元反応に関する
理論的研究

Yohei Kametani

亀谷 陽平

Department of Applied Chemistry
Graduate School of Engineering
Kyushu University

2024

Table of Contents

Chapter 1. General Introduction

1.1. The Nitrogen Cycle

Nitrogen is a vital element for life, being used for the biosynthesis of N-containing compounds (proteins, nucleic acids, and other fundamental compounds).[1] A biosphere ultimately needs to incorporate nitrogen into biological molecules through dinitrogen (N_2) fixation (Figure 1-1), in which bacterial and archaeal prokaryotes convert atmospheric N_2 to ammonium. When organisms die, ammonium is returned to the environment and is sequentially oxidized to nitrate (NO_3^-) via nitrite (NO_2^-), known as nitrification (Figure 1-1). In the absence of oxygen, NO_3^- can be utilized by many microorganisms as a respiratory electron acceptor. In denitrification, NO_3^- is sequentially reduced to N_2 according to the process $NO_3^- \rightarrow NO_2^- \rightarrow$ nitric oxide (NO) $\rightarrow$ nitrous oxide (N_2O) $\rightarrow$ N_2 (Figure 1-1). The four steps in the denitrification process are catalyzed by different metalloenzymes that have a transition metal center as their catalytic active site: molybdenum-dependent nitrate reductase (NaR), heme-containing nitrite reductase (Cd_1NiR) or copper-containing nitrite reductase (CuNiR), heme/non-heme diiron nitric oxide reductase (NOR), and Cu_4S-cluster-containing nitrous oxide reductase (N_2OR).[1b,2] The transition metal center acts as a binding site and electron source and the surrounding amino residue provides protons.

Figure 1-1. Simplified representation of the nitrogen cycle. Denitrification, red arrow; dinitrogen fixation, green arrow; nitrification, blue arrow.

1.2. NO_x Reduction by Functional Metal Complexes

The identification of the active sites of numerous metalloenzymes through crystallographic study motivated researchers to mimic these active sites through the use of metal complexes.[2] The synthesis of inorganic model complexes is conducted on the assumption that the fundamental chemistry of a metal ion remains intact in metalloenzymes. The chemical properties of the active site of a protein are dominated by both the direct and secondary coordination environments surrounding the metal ion. Although the environment of a protein cannot perfectly be mimicked by a synthetic model, one can model the local structure and geometry down to the first or second coordination sphere. Such modeling has led to the synthesis of a variety of mimetic complexes and the development of improved models that are far from natural enzymes in structure. Here, several examples of metal-complex-mediated NO and NO_2^- reductions, which will be described in this dissertation, are introduced.

Reduction of NO to N_2O

There have been several reports on a synthesis of dinuclear metal complex and an examination of its reactivity for the NO reduction. These complexes are similar to natural NORs in having a bimetallic system. However, their reaction mechanisms of NO reduction should be quite different, depending on the type of metal, metal-metal distance, and ligand structure.

Bacterial NORs in denitrification have the heme/nonheme diiron active site, where the nonheme iron is coordinated by three histidine-N atoms.[2] Ju et al. developed the NOR-model diiron complex that possesses porphyrin derivative tethered with tris(2-pyridylmethyl)amine (Figure 1-2, **FeFe1**).[3] A heme/non-heme diiron(II) complex $[Fe^{II}\cdots Fe^{II}]^+$ was prepared and allowed to react with NO at low complex concentrations to give an oxido bridged complex $[Fe^{III}\text{-}O\text{-}Fe^{III}]^+$. This result indicated that the synthetic heme/non-heme complex has the ability to reduce NO to N_2O. Collman et al. reported another biomimetic model of the heme/non-heme diiron motif.[4] They synthesized a porphyrin tethered with three imidazole pickets at the distal site and an imidazole ligand at the proximal site (Figure 1-2, **FeFe2**). This model reacted with 2 equiv. of NO to form 1 equiv. of N_2O. They suggested that the proximal imidazole ligand enhances a radical

character of the iron nitrosyl species during the reaction. In addition to bacterial NORs, flavodiiron nitric oxide reductase (FNOR) facilitates the NO reduction by which some pathogens protect themselves from NO toxicity.[5] FNORs possess the active site of nonheme diiron motif using a flavin mononucleotide cofactor as reducing agent. Lehnert and co-workers reported the FNOR-model diiron complex $[Fe_2(BPMP)(OPr)(NO)_2]^{2+}$ (BPMP = 2,6-bis[(bis(2-pyridylmethyl)amino)methyl]-4-methylphenolate) and showed its ability to reduce NO (Figure 1-2, **FeFe3**).[6]

In addition to the bioinspired models described above, extensive types of dinuclear metal complexes have been developed for the reduction of NO to N_2O. Alkoxylate-bridged diiron complexes (Figure 1-2, **FeFe4** and **FeFe5**) are analogues of the FNOR-model complex **FeFe3** and were used to the NO reduction. **FeFe4** exhibited the conversion of NO to N_2O without any reductants.[7] Crystallographic studies showed an N_2O_2-bridged tetrairon complex, having 2 equiv. of **FeFe4** and 2 equiv. of NO. The reaction pathway was proposed to generate N_2O through the intermolecular N–N bond coupling between two nitrosyl complexes to form the N_2O_2-bridged tetrairon complex. **FeFe5** represents an extended form of **FeFe4**, in which four benzimidazolyl groups are introduced.[8] In contrast to **FeFe4**, **FeFe5** required a reductant (cobaltocene; $Co(\eta^5\text{-}C_5H_5)_2$) for the generation of N_2O and the corresponding N_2O_2-bridged tetrairon complex have not been observed. Therefore, **FeFe5** is assumed to perform the intramolecular N–N bond coupling.

Dicopper complexes (Figure 1-2, **CuCu1** and **CuCu2**) have also been synthesized for NO reduction. The dicopper complex **CuCu1** is the metal center-variant of **FeFe3** and has been reported to perform NO reduction with no proton donors and no reductants.[9] Another dicopper complex ligated with four pyridine ligands linked by catecholate (**CuCu2**) is also capable of reducing NO to N_2O without any additional reagents.[10] The reaction mechanism of **CuCu2** will be described in Chapter 2.

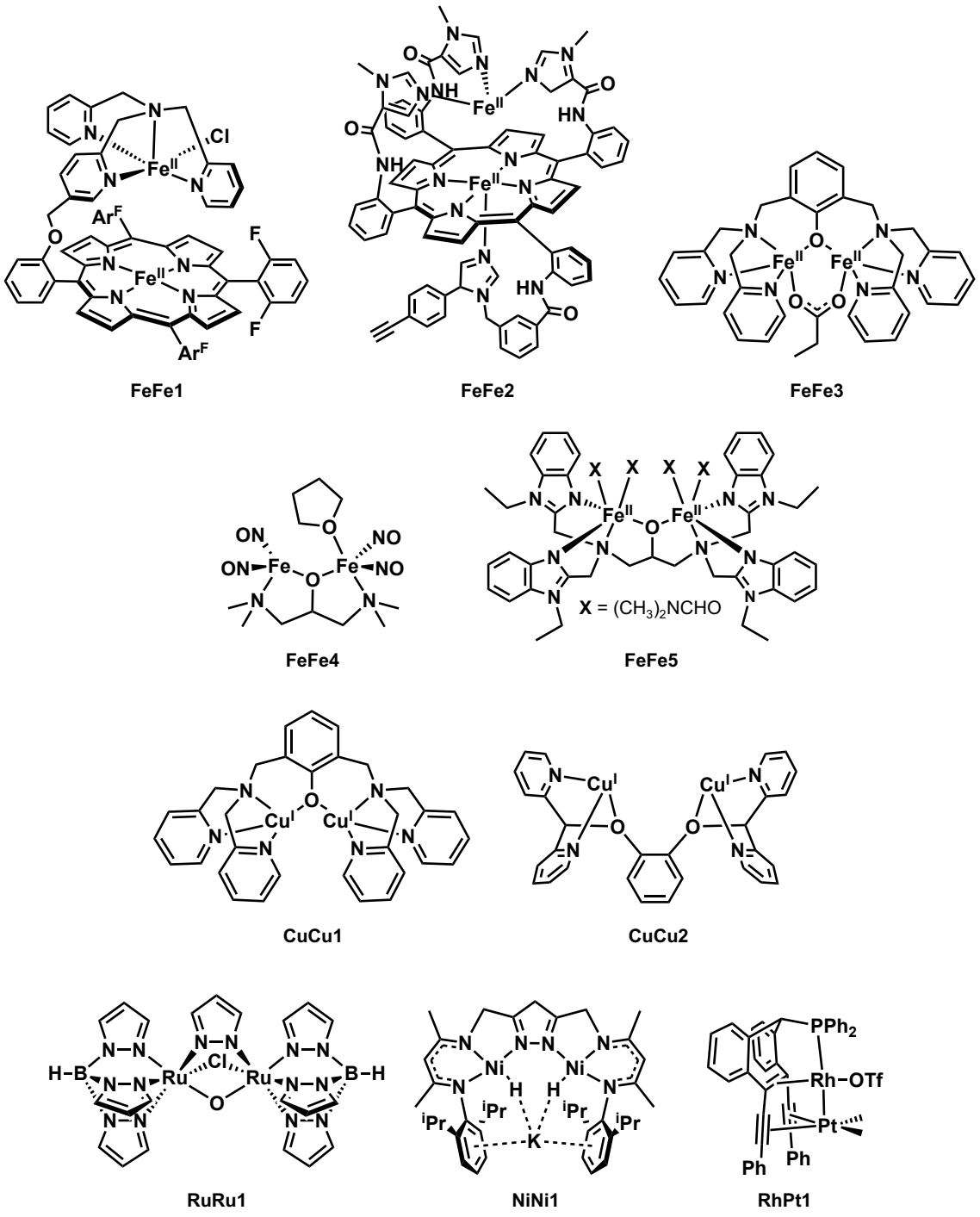

Figure 1-2. Functional metal complexes for the reduction of NO to N_2O.

Other dinuclear metal complexes, which are structurally far from bioinspired models, are also introduced (Figure 1-2, **RuRu1**, **NiNi1**, and **RhPt1**). Among several complexes for NO reduction, a diruthenium complex **RuRu1** is an interesting example, consisting of Cl^{-}, pyrazolato, and two hydrotris(pyrazolyl)borate (Tp) ligands.[11] The reaction of the dinitrosyl complex [Ru_2NO_2] with HBF_4•Et_2O as a proton donor generates N_2O. X-ray crystallography for the dinitrosyl complex revealed a longer N–N bond (1.861(3) Å) compared to the typical N–N single bond (~1.4 Å), indicating a neutral-NO dimer complex [$Ru^{II}_2(NO^0)_2$]. Furthermore, the oxidation of the dinitrosyl complex [$Ru^{II}_2(NO^0)_2$] by $AgBF_4$ resulted in a dicationic dinitrosyl complex $[Ru_2(NO)_2]^{2+}$. The crystallographic result showed a much longer N–N distance (3.006(8) Å) and nearly linear Ru–N–O angles (169.7(6) and 165.4(6)°). Given these results, the electronic structure of the dicationic complex can be assigned as $[Ru^{II}_2(NO^{+})_2]^{2+}$. A dinickel(I) dihydride complex **NiNi1**, which possesses a β-diketiminato-based ligand, has been reported to readily undergo intramolecular H_2 elimination and was therefore described as a potential [Ni^{I}_2] species.[12] The reaction of **NiNi1** with 2 equiv. of NO resulted in [$Ni_2(N_2O_2)$].[13] An X-ray study determined an unusual N,O-bridged-*cis*-N_2O_2 dinickel complex. Subsequent protonation triggered the generation of N_2O. Considering the results of quantum chemical calculations, the presence of K^{+} between two Ph rings could stabilize the N_2O_2 anion and facilitate its isomerization at the dinickel sites. At last, the bimetallic Rh^{I}–Pt^{II} complex reported by Grützmacher and co-workers[14] (**RhPt1**) is one of the few examples of a homogeneous catalyst for the NO reduction. Notably, **RhPt1** is also capable of catalytic reductions of nitrogen dioxide (NO_2) and N_2O to NO and N_2O to N_2, respectively. Given that H_2 was used as a reductant, **RhPt1** would have both abilities of the H_2 activation and the NO_x reduction (hydrogenation).

Reduction of NO_2^- to NO

Tolman and coworkers[15] have developed the first functional model (Figure 1-3, **Cu1**) mimicking the CuNiR T2 site, which possesses the Cu center coordinated by three histidine residues. They utilized a 1,4,7-triazacyclononane (TACN) ligand to replicate a distorted-tetrahedral copper center of the CuNiR T2 site. They showed that the nitrite copper(I) complex, [TACN-$Cu^I(NO_2)$], reacts with acetic acid to yield NO.

Several reports on copper complexes with ligands containing imidazole or benzimidazole have been published. Casella et al.[16] investigated the NO_2^- reduction properties of three Cu(I) complexes with 1-methylbenzimidazole as a ligand (Figure 1-3, **Cu2**, **Cu3**, and **Cu4**). All of them showed the NO_2^- reduction activity in the presence of HBF_4•Et_2O as a proton source, and the order of the NO_2^- reduction activity was **Cu3** > **Cu2** > **Cu4**. In addition, **Cu5**[17] and **Cu6**[18] in Figure 1-3, which have pincer-type ligands containing imidazole, have also been reported to be active for reducing NO_2^-.

In a number of studies, the use of phenol or thiophenol derivatives together with metal complexes (Figure 1-3, **Cu7**, **Cu8**, **Cu9**, and **Fe1**) resulted in the formation of biphenol or diphenyl disulfide, along with NO.[19–22] This suggests that these additives served as proton and electron sources. Notably, the report by Mondal et al. on NO_2 reduction using **Cu7** and a phenol derivative[19] indicated the involvement of proton-coupled electron transfer through kinetic analysis. Chapter 3 will provide a comprehensive discussion of this reaction mechanism.

All of the above reports require a proton source or reducing agent. Conversely, there have been a few examples of NO_2^- reduction without any additives by introducing a proton donor into a ligand. An iron N-confused porphyrin complex (Figure 1-3, **Fe2**) performs NO_2^- reduction without any additive.[23] It is suggested that the C–H and N–H of the inverted pyrrole ring act as a proton donor. Similar to **Fe2**, **Fe3** in Figure 1-3 also achieves additive-free NO_2^- reduction by introducing ammonium bromide as a proton donor into the ligand.[24] An iron(II) complex (**Fe4**) with a tripodal ligand containing a pyrrole ring reduced NO_2^- to NO and produced an iron(III)-oxo complex.[25] The reaction was probably promoted by the attraction of electrons to the NO_2^- ligand by the amino moiety, which is linked to the pyrrole ring, acting as H-bonding donor.

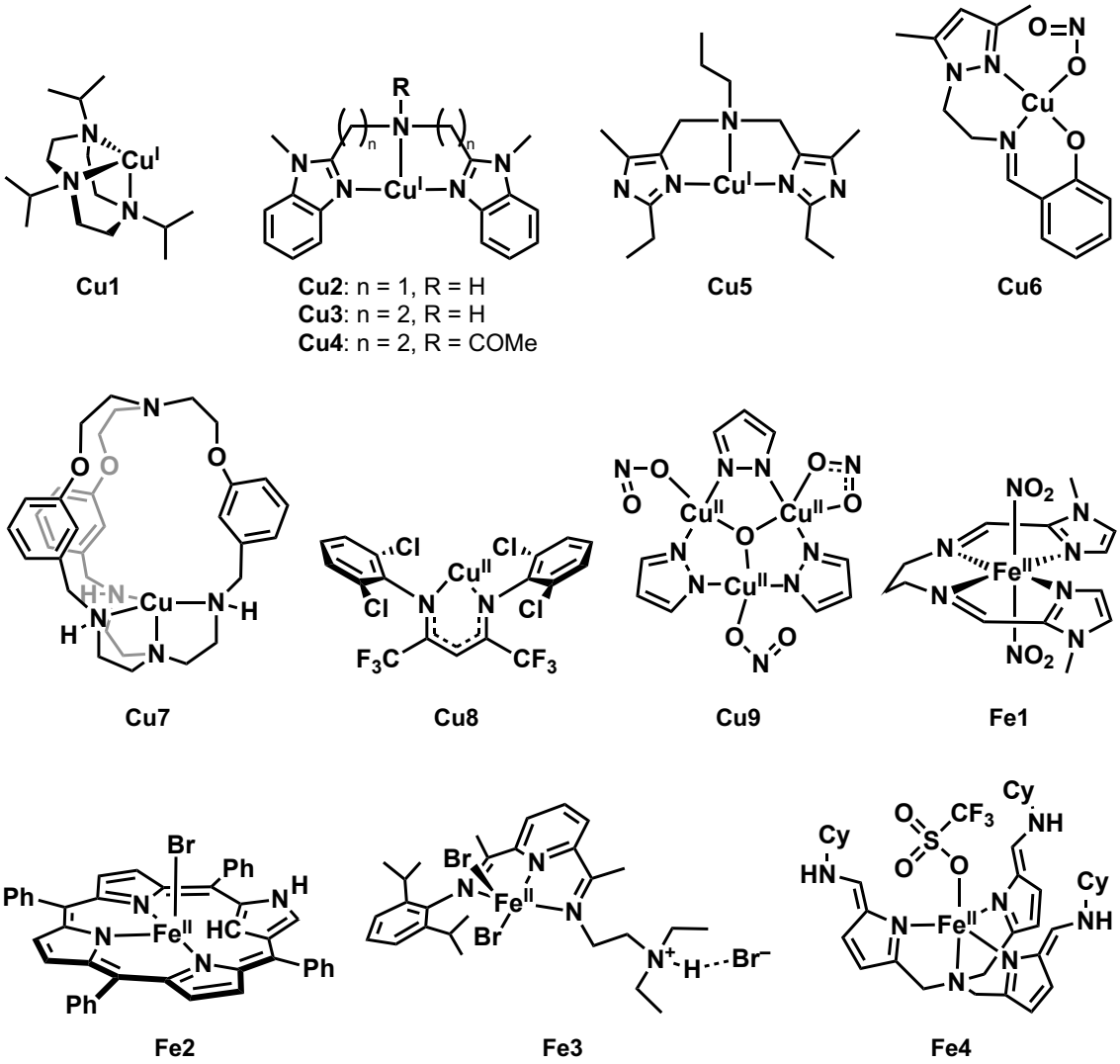

Figure 1-3. Functional metal complexes for the reduction of NO_2^- to NO.

1.3. Reaction Mechanism of Denitrification Reactions

Major structural changes in the denitrification reaction include the cleavage of the N–O bond and the formation of the N–N bond. When the NO_x species receive electrons, the N–O bond elongates and the N–N bond between the NO dimer shortens. This behavior can be explained by the concept of molecular orbital (MO). The lowest unoccupied molecular orbital (LUMO) of NO_3^- and NO_2^- contains the π*(N–O) component (Figure 1-4), which results in a weakening of the N–O bond in response to reduction. In contrast, the LUMO of $(NO)_2$ exhibits the π(N–N) interaction between two π*(N–O) orbitals (Figure 1-4), leading to a strengthening of the N–N bond.

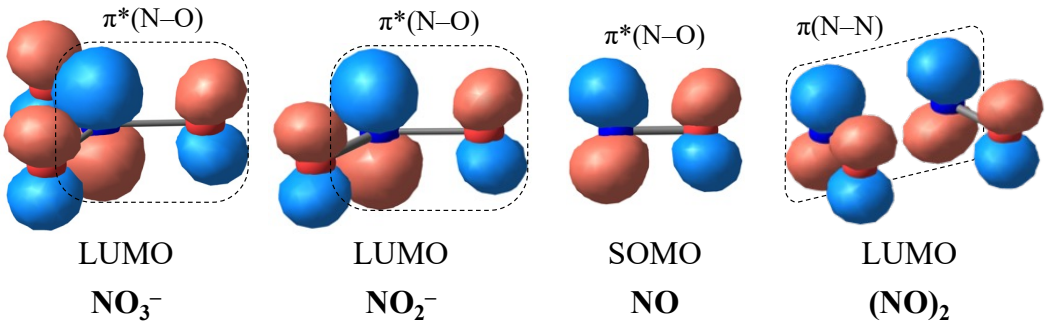

Figure 1-4. Frontier orbitals of NO_3^-, NO_2^-, NO, and the NO dimer. The blue and red balls represent the N and O atoms, respectively.[26]

In addition to the bond behavior, coordination modes of NOx species to metal centers, i.e., N- or O-coordination, significantly contribute to the reaction mechanism. In the enzymatic NO_2^- reduction, crystal structures of Cd_1NiR showed that NO_2^- binds to the iron center in the nitro mode (N-coordination), whereas the nitrite mode (O-coordination) has been detected in CuNiR (Figure 1-5(a)). In the NO reduction (2 NO → N_2O + [O]), various coordination modes of hyponitrite (ONNO) should be considered (Figure 1-5(b)). The ONNO intermediate must adopt the O-coordination mode to form metal-oxo species although NO prefers the N-coordination mode. Note that *cis-trans* isomerization should also be considered in the NO reduction.

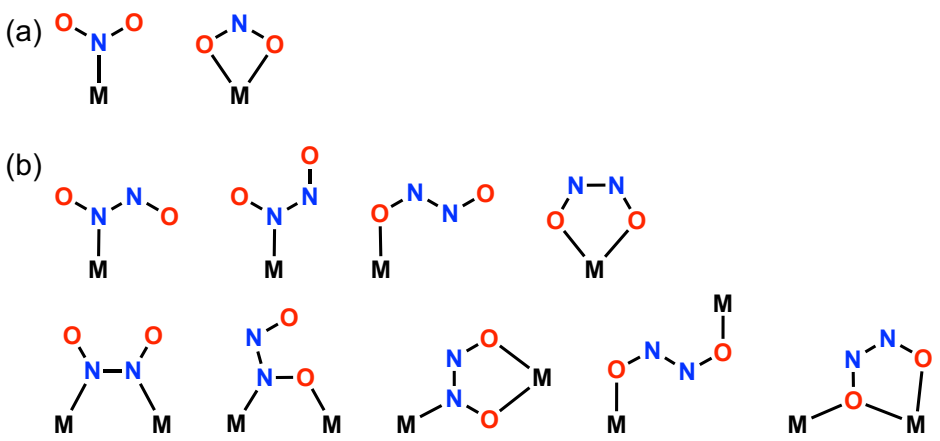

Figure 1-5. Possible binding modes of (a) NO_2^- to the metal atom (**M**) and (b) ONNO to the mono- and di-nuclear center.

1.4. Overview of This Dissertation

The reduction of NO_x plays a significant role in the purification of exhaust gases and groundwater, as well as in the biological denitrification process. A deeper understanding of the reaction mechanism involved in NO_x reduction, including the identification of reaction intermediates, the determination of the rate-limiting step, and the analysis of the critical electronic structures, contributes to the advancement and enhancement of purification catalysts.

Among the NO_x reduction reactions, the NO molecule appears in the reduction of NO_2^- and NO. Since NO has one unpaired electron, the relevant chemical reaction is an open-shell system. Moreover, NO binding to metal ions possesses a non-innocent nature, meaning that it exhibits different oxidation states (NO^+, $^\bullet NO$, or NO^-) depending on the type of metal and other ligands in the metal complex. Thus, the mechanistic analysis of chemical reactions involving NO requires knowledge of bioinorganic chemistry and coordination chemistry, as well as computational chemistry techniques. Due to these difficulties, theoretical studies on the reaction mechanisms of NO and NO_2^- reductions have been limited compared to other small molecule activation reactions, such as O_2 activation and CO_2 reduction.

In this dissertation, the author performed DFT calculations to determine the reaction mechanism of NO_x reduction reactions catalyzed by copper complexes. The theoretical study presented here is not merely an elucidation of individual reaction mechanisms; it also provides sample data that facilitate comparative studies of the reaction mechanisms in the case of various complexes. This approach highlights the unique reaction behaviors and electronic structures shown by different complexes, offering valuable insights for optimizing catalytic performance through molecular design. This dissertation contributes to advancing the understanding of homogeneous NO_x reduction and to accelerating the development of next-generation catalysts in this field.

In Chapter 2 (*Dalton Trans.* **2022**, *51*, 5399-5403), the reaction mechanism fo reduction of NO to N_2O mediated by a dicopper complex is investigated. The computed results indicate that the reaction consists of three fundamental steps: (1) N–N bond formation, (2) isomerization of the N_2O_2 moiety and (3) N–O bond cleavage. The rate-

determining step is the first step of the N–N bond formation, and its activation energy is 21.8 kcal mol^{-1}. During the NO reduction, the dicopper complex possesses various intermediates containing the *cis*- and *trans*-N_2O_2 isomers with different coordination modes to the Cu atoms. This flexibility of the dicopper complex allows adopting the most favored structures for each step in the NO reduction. As a result of electronic structure analysis, the frequent ET between the Cu atoms and the ligand, in addition to the structural flexibility, facilitate the occurrence of the sequential reactions during the NO reduction.

In Chapter 3 (*Inorg. Chem.* **2023**, *62*, 13765-13774), the reduction of NO_2^- to NO mediated by a copper complex using phenol as a reductant is analyzed. Two reaction pathways initiated from O-coordinated nitrite complex (Cu-ONO) and N-coordinated nitro complex (Cu-NO_2) are investigated. Given the calculated energy profiles, the two pathways are comparable. In addition, both pathways involve with concerted proton-electron transfer (CPET). To better understand the CPET-derived NO_2^- reduction, the electronic state changes associated with the structural changes derived from the intrinsic reaction coordinate (IRC) analysis were examined carefully, revealing the behaviors of proton transfer (PT) and electron transfer (ET) along the reaction coordinate. Then, the author introduced the PT and ET points as indices to evaluate the asynchronicity of PT and ET in a CPET reaction. The IRC analysis conducted with PT and ET points revealed the difference of the CPET mechanism in the two pathways substantially in terms of the asynchronicity of PT and ET.

References

1. (a) Fraústo da Silva, J. J. R.; Williams, R. J. P. In *The Biological Chemistry of the Elements: The Inorganic Chemistry of Life*; Oxford University Press: Oxford, 2001. (b) Moura, I., Moura, J. J. G., Pauleta, S. R., Maia, L. B., Eds. *Metalloenzymes in Denitrification: Applications and Environmental Impacts*. Royal Society of Chemistry, 2016. (c) Canfield, D. E.; Glazer, A. N.; Falkowski, P. G. The Evolution and Future of Earth's Nitrogen Cycle. *Science* **2010**, *330*, 192-196.
2. Timmons, A. J.; Symes, M. D. Converting between the Oxides of Nitrogen Using Metal-Ligand Coordination Complexes. *Chem. Soc. Rev.* **2015**, *44*, 6708–6722.
3. Ju, T. D.; Woods, A. S.; Cotter, R. J.; Moënne-Loccoz, P.; Karlin, K. D. Dioxygen and nitric oxide reactivity of a reduced heme/non-heme diiron(II) complex $[(^5L)Fe^{II}\cdots Fe^{II}–Cl]^+$. Using a tethered tetraarylporphyrin for the development of an active site reactivity model for bacterial nitric oxide reductase. *Inorg. Chim. Acta* **2000**, *297*, 362-372.
4. Collman, J. P.; Yang, Y.; Dey, A.; Decréau, R. A.; Ghosh, S.; Ohta, T.; Solomon, E. I. A functional nitric oxide reductase model. *Proc. Natl. Acad. Sci. U.S.A.* **2008**, *105,* 15660-15665.
5. Khatua, S.; Majumdar, A. Flavodiiron nitric oxide reductases: Recent developments in the mechanistic study and model chemistry for the catalytic reduction of NO. *J. Inorg. Biochem*. **2015**, *142*, 145-153.
6. (a) Zheng, S.; Berto, T. C.; Dahl, E. W.; Hoffman, M. B.; Speelman, A. L.; Lehnert, N. The Functional Model Complex $[Fe_2(BPMP)(OPr)(NO)_2](BPh_4)_2$ Provides Insight into the Mechanism of Flavodiiron NO Reductases. *J. Am. Chem. Soc.* **2013**, *135*, 4902-4905. (b) Van Stappen, C.; Lehnert, N. Mechanism of N–N Bond Formation by Transition Metal–Nitrosyl Complexes: Modeling Flavodiiron Nitric Oxide Reductases. *Inorg. Chem.* **2018**, *57*, 4252-4269.
7. (a) Wu, W. Y.; Hsu, C. N.; Hsieh, C. H.; Chiou, T. W.; Tsai, M. L.; Chiang, M. H.; Liaw, W. F. NO-to-$[N_2O_2]^{2–}$-to-N_2O Conversion Triggered by $\{Fe(NO)_2\}^{10}$-$\{Fe(NO)_2\}^9$ Dinuclear Dinitrosyl Iron Complex. *Inorg. Chem.* **2019**, *58*, 9586-9591. (b) Wu, W. Y.; Tsai, M. L.; Lai, Y. A.; Hsieh, C. H.; Liaw, W. F. NO Reduction to N_2O Triggered by a Dinuclear Dinitrosyl Iron Complex via the Associated

Pathways of Hyponitrite Formation and NO Disproportionation. *Inorg. Chem.* **2021**, *60*, 15874-15889.

8. (a) Jana, M.; Pal, N.; White, C. J.; Kupper, C.; Meyer, F.; Lehnert, N.; Majumdar, A. Functional Mononitrosyl Diiron(II) Complex Mediates the Reduction of NO to N_2O with Relevance for Flavodiiron NO Reductases. *J. Am. Chem. Soc.* **2017**, *139*, 14380-14383. (b) Jana, M.; White, C. J.; Pal, N.; Demeshko, S.; Cordes, C.; Meyer, F.; Lehnert, N.; Majumdar, A. Functional Models for the Mono- and Dinitrosyl Intermediates of FNORs: Semireduction versus Superreduction of NO. *J. Am. Chem. Soc.* **2020**, *142*, 6600-6616.
9. Paul, P. P.; Karlin, K. D. Functional modeling of copper nitrite reductases: reactions of NO_2^- or nitric oxide with copper(I) complexes. *J. Am. Chem. Soc.* **1991**, *113*, 6331-6332.
10. Tao, W.; Bower, J. K.; Moore, C. E.; Zhang, S. Dicopper μ-Oxo, μ-Nitrosyl Complex from the Activation of NO or Nitrite at a Dicopper Center. *J. Am. Chem. Soc.* **2019**, *141*, 10159-10164.
11. (a) Arikawa, Y.; Asayama, T.; Moriguchi, Y.; Agari, S.; Onishi, M. Reversible N－N Coupling of NO Ligands on Dinuclear Ruthenium Complexes and Subsequent N_2O Evolution: Relevance to Nitric Oxide Reductase. *J. Am. Chem. Soc.* **2007**, *129*, 14160-14161. (b) Arikawa, Y.; Matsumoto, N.; Asayama, T.; Umakoshi, K.; Onishi, M. Conversion of oxido-bridged dinuclear ruthenium complex to dicationic dinitrosyl ruthenium complex using proton and nitric oxide: Completion of NO reduction cycle. *Dalton Trans.* **2011**, *40*, 2148-2150.
12. Duan, P. C.; Manz, D. H.; Dechert, S.; Demeshko, S.; Meyer, F. Reductive O_2 Binding at a Dihydride Complex Leading to Redox Interconvertible μ-1,2-Peroxo and μ-1,2-Superoxo Dinickel(II) Intermediates. *J. Am. Chem. Soc.* **2018**, *140*, 4929-4939.
13. Ferretti, E.; Dechert, S.; Demeshko, S.; Holthausen, M. C.; Meyer, F. Reductive Nitric Oxide Coupling at a Dinickel Core: Isolation of a Key cis-Hyponitrite Intermediate en route to N_2O Formation. *Angew. Chem., Int. Ed.* **2019**, *58*, 1705-1709.
14. Jurt, P.; Abels, A. S.; Gamboa-Carballo, J. J.; Fernández, I.; Le Corre, G.; Aebli,

M.; Baker, M. G.; Eiler, F.; Müller, F.; Wörle, M.; Verel, R.; Gauthier, S.; Trincado, M.; Gianetti, T. L.; Grützmacher, H. Reduction of Nitrogen Oxides by Hydrogen with Rhodium(I)–Platinum(II) Olefin Complexes as Catalysts. *Angew. Chem., Int. Ed.* **2021**, *60*, 25372-25380.

15. Halfen, J. A.; Mahapatra, S.; Wilkinson, E. C.; Gengenbach, A. J.; Young, V. G., Jr.; Que, L., Jr.; Tolman, W. B. Synthetic Modeling of Nitrite Binding and Activation by Reduced Copper Proteins. Characterization of Copper(I)－Nitrite Complexes That Evolve Nitric Oxide. *J. Am. Chem. Soc.* **1996**, *118*, 763-776.
16. Casella, L.; Carugo, O.; Gullotti, M.; Doldi, S.; Frassoni, M. Synthesis, Structure, and Reactivity of Model Complexes of Copper Nitrite Reductase. *Inorg. Chem.* **1996**, *35*, 1101-1113.
17. Beretta, M.; Bouwman, E.; Casella, L.; Driessen, W. L.; Gutierrez-Soto, L.; Monzani, E.; Douziech, B.; Reedijk, J. Copper complexes of a new tridentate imidazole-containing ligand: spectroscopy, structures and nitrite reductase reactivity The molecular structures of [Cu(biap)$(NO_2)_2$] and [Cu(biap)Br_2]. *Inorg. Chim. Acta* **2000**, *310*, 41-50.
18. Maria, S.; Chattopadhyay, T.; Ananya, S.; Kundu, S. Reduction of Nitrite to NO at a Mononuclear Copper(II)-Phenolate Site. *Inorg. Chim. Acta* **2020**, *506*, 119515.
19. Mondal, A.; Reddy, K. P.; Bertke, J. A.; Kundu, S. Phenol Reduces Nitrite to NO at Copper(II): Role of a Proton-Responsive Outer Coordination Sphere in Phenol Oxidation. *J. Am. Chem. Soc.* **2020**, *142*, 1726-1730.
20. Kundu, S.; Kim, W. Y.; Bertke, J. A.; Warren, T. H. Copper(II) Activation of Nitrite: Nitrosation of Nucleophiles and Generation of NO by Thiols. *J. Am. Chem. Soc.* **2017**, *139*, 1045-1048.
21. Shi, K.; Mathivathanan, L.; Boudalis, A. K.; Turek, P.; Chakraborty, I.; Raptis, R. G. Nitrite Reduction by Trinuclear Copper Pyrazolate Complexes: An Example of a Catalytic, Synthetic Polynuclear NO Releasing System. *Inorg. Chem.* **2019**, *58*, 7537-7544.
22. Sanders, B. C.; Hassan, S. M.; Harrop, T. C. NO2- Activation and Reduction to NO by a Nonheme Fe$(NO_2)_2$ Complex. *J. Am. Chem. Soc.* **2014**, *136*, 10230-10233.
23. Ching, W.-M.; Chuang, C.-H.; Wu, C.-W.; Peng, C.-H.; Hung, C.-H. Facile Nitrite

Reduction and Conversion Cycle of {Fe(NO)}$^{6/7}$ Species: Chemistry of Iron N-Confused Porphyrin Complexes via Protonation/Deprotonation. *J. Am. Chem. Soc.* **2009**, *131*, 7952-7953.

24. Kwon, Y. M.; Delgado, M.; Zakharov, L. N.; Seda, T.; Gilbertson, J. D. Nitrite reduction by a pyridinediimine complex with a proton-responsive secondary coordination sphere. *Chem. Commun.* **2016**, *52*, 11016-11019.
25. Matson, E. M.; Park, Y. J.; Fout, A. R. Facile Nitrite Reduction in a Non-Heme Iron System: Formation of an Iron(III)-Oxo. *J. Am. Chem. Soc.* **2014**, *136*, 17398-17401.
26. Molecular orbitals were calculated at the B3LYP/6-311G** level of theory.

Chapter 2. Mechanistic Study on Reduction of Nitric Oxide to Nitrous Oxide Using A Dicopper Complex

2.1. Introduction

The reduction of nitric oxide (NO) to nitrous oxide (N_2O) is important in biological denitrification and in heterogeneous catalytic processes useful for pollution control.[1–3] In biological systems, this reaction is accomplished by NO reductase (NOR) and flavodiiron NO reductase (FNOR), which convert 2 equiv. of NO, two electrons, and two protons into N_2O and water.[3–15] Extensive efforts have been devoted to fully elucidating the corresponding catalytic cycle. On the basis of experimental evidence, NO reduction is widely acknowledged to proceed via a hyponitrite ($N_2O_2^{2-}$) intermediate via N–N bond formation.[16–23] Another useful clue in unraveling the mechanism is a μ-oxo bridged species (*M*–O–*M*), which has been characterized as the resting state of NOR.[24,25] Still, details of the N–N bond formation, N–O bond cleavage, various possible intermediate species, and the exact timing of metal redox shuttling remain elusive.[26–35] Uncovering such details would provide substantial insights for the design of NOR-related therapeutics as well as for improving NOx purification systems.[36–42]

The reduction of NO to N_2O using mono-[43–47] and dicopper[22,48] complexes has been

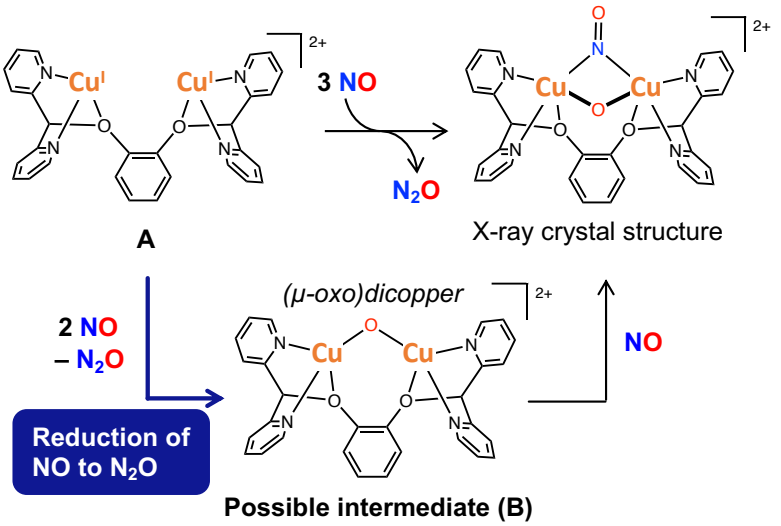

Figure 2-1. Possible reaction pathway of the reduction of NO to N_2O using dicopper complex **A**.

experimentally demonstrated using information obtained from modeling studies. For example, Zhang and co-workers[49] have reported that NO can be activated by the dicopper complex supported by 1,2-bis(di(pyridin-2-yl)methoxy)benzene (**A**). The reaction of **A** with 3 equiv. of NO provides the (μ-oxo)(μ-nitrosyl)dicopper complex and N_2O (Figure 2-1). Possible reaction mechanisms based on measured kinetics and isolated intermediates have been postulated. Metz[50] used density functional theory (DFT) calculations to theoretically investigate the reduction of NO to N_2O by monocopper complexes.[44–46] However, in the case of dicopper complexes, the literature contains no studies that present a complete mechanism including all intermediates. We were therefore motivated to propose a reaction mechanism using a dicopper model for the reduction of NO. In a reduction of NO to N_2O using a bimetallic complex, the μ-oxo complex is generally considered an intermediate or a product. Therefore, the presumed reaction pathway is that dicopper complex **A** reacts with 2 equiv. of NO to form μ-oxo complex **B**, followed by another NO coordinating to **B** to give the product complex (Figure 2-1). In the present study, we focus on the reduction of NO to form N_2O and **B**.

2.2. Computational Methods

All calculations were performed using the spin-unrestricted B3LYP functional[51] implemented in the Gaussian 16 package[52] for the structural optimization. Because the total charge of dicopper(I) complex **A** is +2, we considered three possible spin states: closed-shell singlet, open-shell singlet, and triplet states. The open-shell singlet state was computed using the broken-symmetry approach. Vibration frequencies were systematically computed to ensure that the potential energy surface for each optimized geometry corresponded to a local minimum with no imaginary frequencies, or to a saddle point with only one imaginary frequency. We used the (16*s*10*p*6*d*) primitive set of Wachters–Hay supplemented with one polarization *f*-function (α = 1.44 for Cu)[53] for the Cu atoms and the D95** basis set for the H, C, N, and O atoms.[54] We added the Gibbs free energy correction (T = 298.15 K) and the Grimme's dispersion correction (D3).[55] Implicit solvent effects of tetrahydrofuran (ε = 7.4257) were included via the polarizable continuum model (PCM).[56]

2.3. Results and Discussion

The reaction mechanism and ET proposed on the basis of the calculations are depicted in Figure 2-2. The reaction comprises three steps: (1) N–N bond formation, (2) isomerization of N_2O_2, and (3) N–O bond cleavage. The DFT calculations suggested that the potential energy surfaces of the closed-shell singlet, open-shell singlet, and triplet states lie close together along the first half of the reaction path. In the first step, the three spin states compete energetically. After formation of the N–N bond, the closed-shell singlet is dominant for the isomerization of the N_2O_2 moiety. In the final step, the open-shell singlet and triplet states are low-lying states. The calculated binding energy between **A** and 2 equiv. of NO is −20.2 kcal/mol to form **1** with the end-on coordination mode. In the triplet state of **1**, the N^a–O^a and N^b–O^b bond lengths were calculated to be 1.177 Å and 1.176 Å, respectively. The N^a–N^b distance of 3.815 Å is too far for the two N atoms to interact. The Cu–Cu distance of 4.454 Å is also too far. The computed spin densities of the Cu atoms in **1 (t)** are nearly zero, and the spin densities are spatially localized at the two NO moieties. Thus, the formal charges of the Cu^a and Cu^b atoms can both be assigned as +1 ($3d^{10}$). Given that the relative energies are –1.0 kcal/mol in the open-shell singlet state and +5.4 kcal/mol in the closed-shell singlet state, the other two spin states in **1** are also energetically possible. The optimized geometry of **1 (oss)** is similar to the triplet geometry, and the N^a–N^b distance is 3.319 Å, whereas **1 (css)** has a short N^a–N^b distance of 1.918 Å.

The N^a–N^b bond formation occurs through a transition state, $\mathbf{TS_{1/2}}$. The coordination of the two NO moieties subsequently changes from the end-on mode to the side-on mode, resulting in the two Cu–O bonds in **2**. The N^a–N^b distance decreases from 3.815 Å in **1** to 1.339 Å in **2** via 1.772 Å in $\mathbf{TS_{1/2}}$ in the triplet state. Given the lengths of the N^a–N^b, N^a–O^a, and N^b–O^b bonds, the N_2O_2 moiety of **2** is assigned as the mono-anion $N_2O_2^-$, indicating that one electron was transferred from the dicopper center to the N_2O_2 moiety. The activation energies for $\mathbf{TS_{1/2}}$ are 24.6 kcal/mol in the closed-shell singlet state and 21.8 kcal/mol in the triplet state. Accordingly, the triplet state is dominant to facilitate N–N bond formation. During the reaction from **1 (t)** to $\mathbf{TS_{1/2}}$ **(t)**, there is little change in spin densities is little (see Table S2-2), while the N^a–N^b distance decreases drastically, almost

forming a single N–N bond. Therefore, the shortening of N–N distance, rather than electron transfer, triggers the N–N bond formation.

Subsequently, isomerization of the N_2O_2 ligand with rotation around the N–N bond occurs via **TS$_{2/3}$**, which is a transition state corresponding to the cleavage of the Cu^b–N^b bond and the formation of the Cu^b–O^a bond. In the closed-shell singlet state, the Cu^b–N^b bond distance increases from 1.910 Å in **2** to 2.679 Å in **3** via 2.378 Å in **TS$_{2/3}$**, whereas

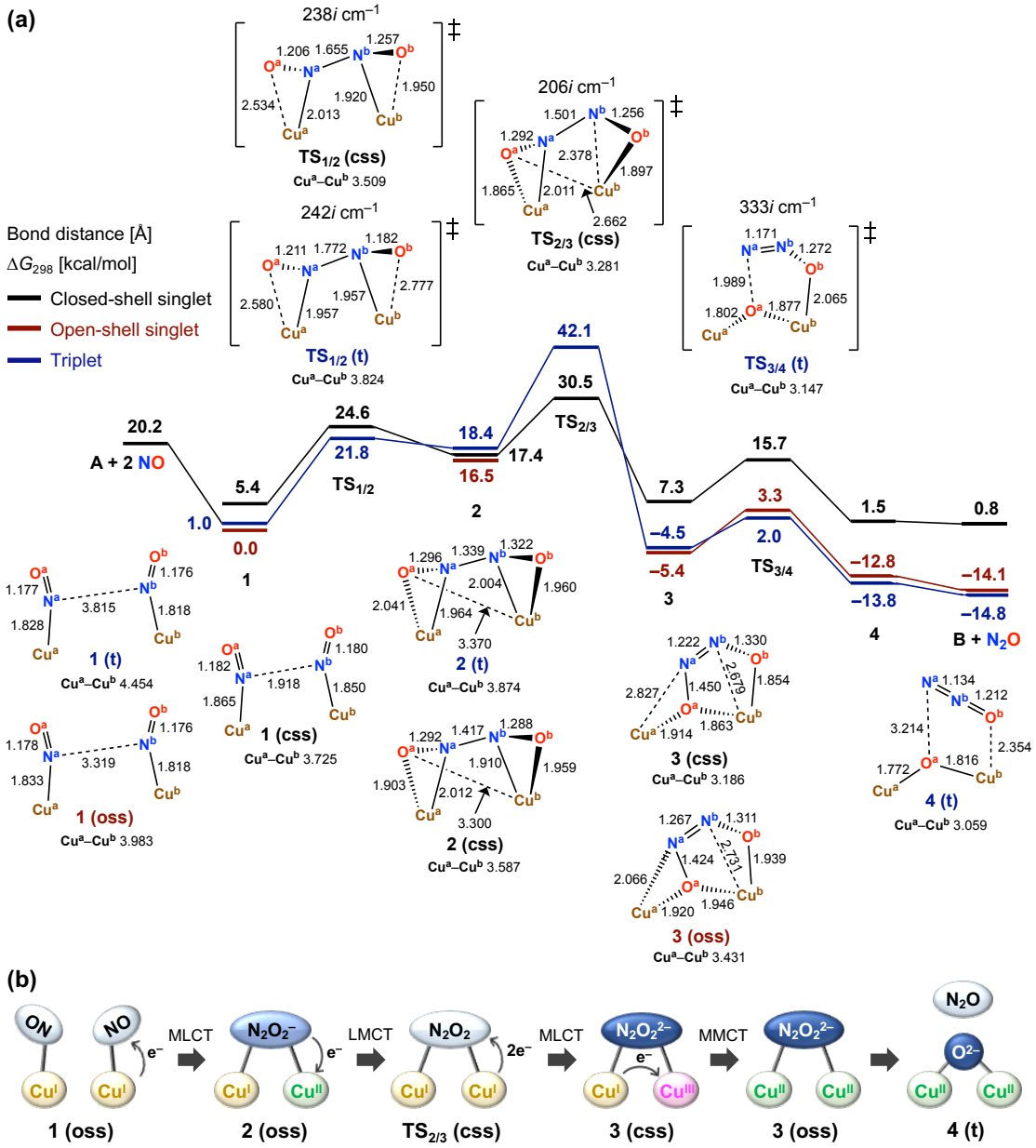

Figure 2-2. (a) Free-energy profile for the reduction of NO to N_2O by dicopper complex **A**. (b) Schematic representation of the changes in electronic states during the NO reduction by the dicopper complex.

the Cu^b–O^a bond distance decreases from 3.300 Å in **2** to 1.946 Å in **3** via 2.662 Å in **$TS_{2/3}$**. This step also corresponds to the *cis–trans* isomerization with respect to the O^a–N^a–N^b–O^b dihedral angle, which decreases from 154.4° in **2** to 3.6° in **3** via 75.8° in **$TS_{2/3}$**. Calculated energies of **$TS_{2/3}$** are 42.1 kcal/mol in the triplet state and 30.5 kcal/mol in the closed-shell singlet state. Thus, the singlet pathway is energetically favored, leading to the formation of **3**. The DFT calculations indicate that electron transfer occurs from the Cu center to the N_2O_2 moiety. In fact, the N^a–N^b bond distance decreases from 1.344 Å in **2** to 1.267 Å in **3** via 1.501 Å in **$TS_{2/3}$**. The N^a–N^b bond is shortened during the step from **2** to **3**, whereas it is elongated in the vicinity of **$TS_{2/3}$**. Such a change of the N^a–N^b bond length represents a decrease in the π-character of the N^a–N^b bond, which facilitates the *trans–cis* rotation. After **$TS_{2/3}$**, the ground state of **3** changes from the closed-shell singlet to the triplet state. To help the better understanding of the change in the electronic state induced by the isomerization, we performed an orbital analysis. Figure 2-3(a) shows an orbital analysis of the isolate N_2O_2 molecule with the dihedral angle of 75.8˚ and **$TS_{2/3}$ (css)**. Structurally compared with the isolate N_2O_2 species (Figure S2-2), the N_2O_2 moiety of dicopper complexes was assigned to mono anion in **2**, neutral molecule in **$TS_{2/3}$** and dianion in **3**. The orbital analysis of **$TS_{2/3}$** shows that the occupied orbital of **$TS_{2/3}$** has the same σ(N–N) orbital as the neutral N_2O_2 molecule. Furthermore, similarities were observed for other orbitals, π(N–N) and π*(N–N), indicating that **$TS_{2/3}$** and the neutral N_2O_2 molecule have a similar electronic configuration (Figure 2-3(b)). Thus, our DFT calculations suggest that the valence of the dicopper active site changes from Cu(I)Cu(II) in **2** to Cu(II)Cu(II) or Cu(I)Cu(III) in **3** via Cu(I)Cu(I) in **$TS_{2/3}$**. Given these geometrical and electronic changes through **$TS_{2/3}$ (css)**, the return of electron to the Cu atoms induces the loosening of the N–N bond, facilitating the *trans–cis* rotation as illustrated in Figure 2-3(c). The closed-shell singlet state and the open-shell singlet state of **3** correspond to Cu(I)Cu(III) and Cu(II)Cu(II), respectively. The disproportionate valence of Cu^a and Cu^b is energetically unfavorable for **3**; thus, one electron is transferred to form the open-shell singlet state of the two Cu(II) centers, as shown in Figure 2-2(b). Notably, it is also plausible that the process proceeds without passing through **3 (css)** (Cu(I)Cu(III)). In this scenario, **$TS_{2/3}$ (css)** (Cu(I)Cu(I)) directly transforms into **3 (oss)** (Cu(II)Cu(II)), where two electrons are transferred from Cu(I)Cu(I)—one from each Cu(I)—to the N_2O_2 ligand.

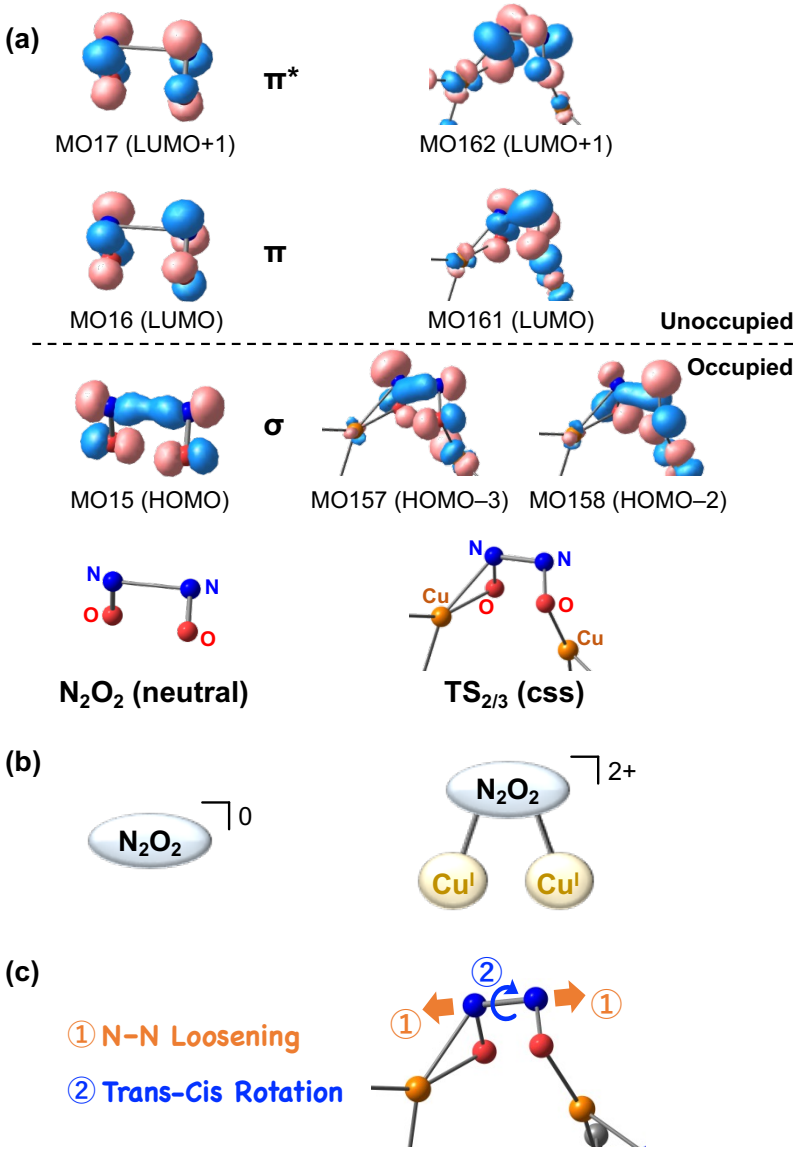

Figure 2-3. Assignment of an electronic structure of **$TS_{2/3}$ (css)**. (a) Molecular orbitals of N_2O_2 molecule and **$TS_{2/3}$ (css)**. The N_2O_2 molecule was produced by rotating the O–N–N–O dihedral angle of the optimized *cis*-N_2O_2 molecule to 75.8°. (b) Schematic representation of formal charges. (c) Conceptual representation of the *trans–cis* rotation via **$TS_{2/3}$ (css)**.

The geometrical structure of **3** is unique, where the N_2O_2 moiety coordinates to the two Cu ions to form a μ-oxo structure. On the basis of the Mulliken spin densities, we assigned the formal charges of the Cu^a and Cu^b atoms and the N_2O_2 moiety in **3 (oss), (t)** as +2, +2, and −2, respectively. Notably, as shown in Figure 2-4, the N^a–O^a bond of **3** is distinctively elongated to 1.424 Å in **3 (oss)**, which is longer than the N–O bond of the *cis*-$N_2O_2^{2-}$ dianion (calculated to be 1.362 Å, see Figure S2-2). A similar intermediate has been reported in the NO reduction by a diiron complex, which is a model of FNOR.[57]

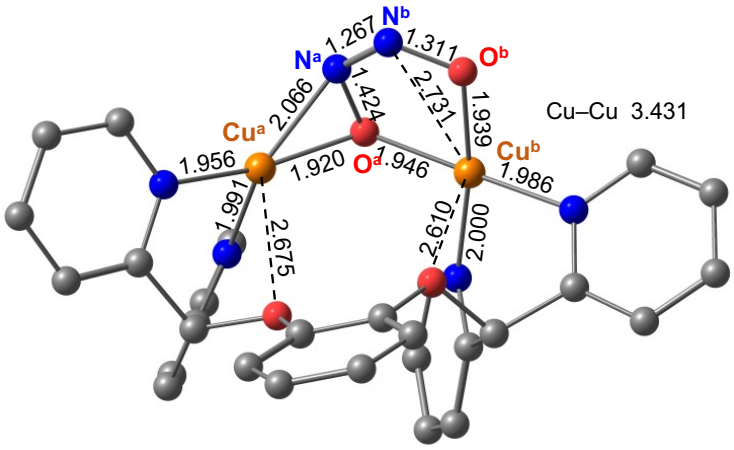

Figure 2-4. Optimized structure of **3 (oss)**. Bond lengths are given in a unit of Å.

In the final step, N^a–O^a bond cleavage occurs to provide the (μ-oxo)dicopper(II) complex and an N_2O molecule. During the N^a–O^a bond cleavage, the N^a–N^b and N^b–O^b bonds shorten and the N^a–N^b–O^b geometry changes from bent to linear. In addition, the Cu–Cu distance is further shortened (3.059 Å in **4 (t)**) to form a μ-oxo bridge. The open-shell singlet and triplet states are dominant in this step because **$TS_{3/4}$ (oss)** and **$TS_{3/4}$ (t)** are lower in energy by 12.4 and 13.7 kcal/mol than **$TS_{3/4}$ (css)**, respectively. The activation energies of **$TS_{3/4}$** are 6.5 kcal/mol in the triplet state and 8.7 kcal/mol in the open-shell singlet state. In the N^a–O^a bond cleavage, the Mulliken charges of the two Cu atoms remain unchanged. The charge of the O^a atom decreases from −0.40 to −0.59, whereas the total charges of the N^a, N^b, and O^b atoms increase from –0.17 to 0.12. Therefore, this step is completed by the electron transfer from the N^a, N^b, and O^b atoms to the O^a atom. In **4**, the open-shell singlet and triplet states are stable and no significant differences in geometry or energy are observed. The spin density of the N_2O moiety is almost zero. Accordingly, the $N^aN^bO^b$ moiety exists as the N_2O molecule, indicating that

little interaction occurs between the (μ-oxo)dicopper complex and the N_2O molecule. Finally, the desorption energy of N_2O from **4** requires 7.4 kcal/mol (electronic energy) to give the (μ-oxo)dicopper complex **B** in the triplet state. However, the desorption energy becomes unnecessary when entropy correction is considered, as shown in Figure 2-2(a).

The overall reaction proceeds exothermically with an energy of 35.0 kcal/mol. The rate-determining step is the first step of the N–N bond formation, and its activation energy is 21.8 kcal/mol. During the NO reduction, the dicopper complex possesses various intermediates containing the *cis*- and *trans*-N_2O_2 isomers with different coordination modes to the Cu atoms. This flexibility of the dicopper complex allows adopting the most favored structures for each step in the NO reduction, i.e., N–N bond formation, N_2O_2 isomerization, and N–O bond cleavage. In addition to this structural flexibility, the frequent ET between the Cu atoms and the ligand, as illustrated in Figure 2-2(b), facilitate the occurrence of the sequential reactions during the NO reduction.

2.4. Conclusions

We have investigated the mechanism for the reduction of NO to N_2O by a dicopper complex using DFT calculations. The computed results indicate that the reaction consists of three fundamental steps: (1) N–N bond formation, (2) isomerization of the N_2O_2 moiety and (3) N–O bond cleavage. The calculated reaction mechanism predicts that the coupling of two NO molecules initially occurs. The two NO molecules then transform from the end-on to the side-on mode. The first step requires an activation energy of 21.8 kcal/mol in the triplet state and is the rate-determining step in this mechanism. The *cis–trans* isomerization of the N_2O_2 moiety then occurs as the O atom is bridged between two Cu atoms with an activation energy of 13.1 kcal/mol in the closed-shell singlet state. Finally, cleavage of the N–O bond occurs to give $[Cu_2(\mu\text{-}O)]^{2+}$ with N_2O. The elongated N–O bond in the reaction intermediate $[Cu_2(\mu\text{-}ONNO)]^{2+}$ contributes to the small activation energy of only 6.5 kcal/mol in the triplet state. The overall reaction was calculated to be exothermic by 35.0 kcal/mol in the triplet state. These computed results are consistent with the experimental observation, where N_2O is released using the dicopper complex. In addition, the large binding energy of NO and Cu atoms in the reactant complex $[Cu_2(NO)_2]^{2+}$ and the small binding energy of N_2O in the product complex $[Cu_2(N_2O)(\mu\text{-}O)]^{2+}$ favor this catalytic cycle.

References

1. Ferousi, C.; Majer, S. H.; DiMucci, I. M.; Lancaster, K. M. Biological and Bioinspired Inorganic N-N Bond-Forming Reactions. *Chem. Rev.* **2020**, *120*, 5252-5307.
2. Granger, P.; Parvulescu, V. I. Catalytic NO_x Abatement Systems for Mobile Sources: From Three-Way to Lean Burn after-Treatment Technologies. *Chem. Rev.* **2011**, *111*, 3155-3207.
3. Wasser, I. M.; Vries, S.; Moënne-Loccoz, P.; Schröder, I.; Karlin, K. D. Nitric oxide in biological denitrification: Fe/Cu metalloenzyme and metal complex NOx redox chemistry. *Chem. Rev.* **2002**, *102*, 1201-1234.
4. Wang, J.; Schopfer, M. P.; Puiu, S. C.; Sarjeant, A. A. N.; Karlin, K. D. Reductive Coupling of Nitrogen Monoxide (•NO) Facilitated by Heme/Copper Complexes. *Inorg. Chem.* **2010**, *49*, 1404-1419.
5. Hayashi, T.; Caranto, J. D.; Wampler, D. A.; Kurtz, D. M., Jr.; Moënne-Loccoz, P. Insights into the Nitric Oxide Reductase Mechanism of Flavodiiron Proteins from a Flavin-Free Enzyme. *Biochemistry* **2010**, *49*, 7040-7049.
6. Hayashi, T.; Caranto, J. D.; Matsumura, H.; Kurtz, D. M., Jr.; Moënne-Loccoz, P. Vibrational Analysis of Mononitrosyl Complexes in Hemerythrin and Flavodiiron Proteins: Relevance to Detoxifying NO Reductase. *J. Am. Chem. Soc.* **2012**, *134*, 6878-6884.
7. Kurtz, D. M., Jr. Flavo-diiron enzymes: nitric oxide or dioxygen reductases? *Dalton Trans.* **2007**, *37*, 4115-4121.
8. Silaghi-Dumitrescu, R.; Coulter, E. D.; Das, A.; Ljungdahl, L. G.; Jameson, G. N. L.; Huynh, B. H.; Kurtz, D. M., Jr. A flavodiiron protein and high molecular weight rubredoxin from Moorella thermoacetica with nitric oxide reductase activity. *Biochemistry* **2003**, *42*, 2806-2815.
9. Schopfer, M. P.; Wang, J.; Karlin, K. D. Bioinspired Heme, Heme/Nonheme Diiron, Heme/Copper, and Inorganic NOx Chemistry: •NO(g) Oxidation, Peroxynitrite-Metal Chemistry, and •NO(g) Reductive Coupling. *Inorg. Chem.* **2010**, *49*, 6267-6282.
10. Wang, J.; Schopfer, M. P.; Sarjeant, A. A. N.; Karlin, K. D. Heme-Copper Assembly

Mediated Reductive Coupling of Nitrogen Monoxide (•NO). *J. Am. Chem. Soc.* **2009**, *131*, 450-451.

11. Ju, T. D.; Woods, A. S.; Cotter, R. J.; Moënne-Loccoz, P.; Karlin, K. D. Dioxygen and nitric oxide reactivity of a reduced heme/non-heme diiron(II) complex $[(^5L)Fe^{II}...Fe^{II}\text{-}Cl]^+$: Using a tethered tetraarylporphyrin for the development of an active site reactivity model for bacterial nitric oxide reductase. *Inorg. Chim. Acta* **2000**, *297*, 362-372.
12. Collman, J. P.; Yang, Y.; Dey, A.; Decraeau, R. A.; Ghosh, S.; Ohta, T.; Solomon, E. I. A functional nitric oxide reductase model. *Proc. Natl. Acad. Sci. U.S.A.* **2008**, *105*, 15660-15665.
13. Collman, J. P.; Dey, A.; Yang, Y.; Decraeau, R. A.; Ohta, T.; Solomon, E. I. Intermediates Involved in the Two Electron Reduction of NO to N_2O by a Functional Synthetic Model of Heme Containing Bacterial NO Reductase. *J. Am. Chem. Soc.* **2008**, *130*, 16498-16499.
14. Collman, J. P.; Yan, Y.-L.; Lei, J.; Dinolfo, P. H. Active-site models of bacterial nitric oxide reductase featuring tris-histidyl and glutamic acid mimics: Influence of a carboxylate ligand on Fe_B binding and the heme Fe/Fe_B redox potential. *Inorg. Chem.* **2006**, *45*, 7581-7583.
15. Zheng, S.; Berto, T. C.; Dahl, E. W.; Hoffman, M. B.; Speelman, A. L.; Lehnert, N. The Functional Model Complex $[Fe_2(BPMP)(OPr)(NO)_2](BPh_4)_2$ Provides Insight into the Mechanism of Flavodiiron NO Reductases. *J. Am. Chem. Soc.* **2013**, *135*, 4902-4905.
16. Brown, W. A.; Gardner, P.; King, D. A. Very Low Temperature Surface Reaction: N_2O Formation from NO Dimers at 70 to 90 K on Ag{111}. *J. Phys. Chem.* **1995**, *99*, 7065-7074.
17. Brown, W. A.; King, D. A. NO chemisorption and reactions on metal surfaces: A new perspective. *J. Phys. Chem. B* **2000**, *104*, 2578-2595.
18. Shiotari, A.; Kitaguchi, Y.; Okuyama, H.; Hatta, S.; Aruga, T. Imaging Covalent Bonding between Two NO Molecules on Cu(110). *Phys. Rev. Lett.* **2011**, *106*, 156104.
19. Shiotari, A.; Hatta, S.; Okuyama, H.; Aruga, T. Formation of unique trimer of nitric

oxide on Cu(111). *J. Chem. Phys.* **2014**, *141*, 134705.

20. Hess, C.; Ozensoy, E.; Yi, C.-W.; Goodman, D. W. NO dimer and dinitrosyl formation on Pd(111): From ultra-high-vacuum to elevated pressure conditions. *J. Am. Chem. Soc.* **2006**, *128*, 2988-2994.
21. Varotsis, C.; Ohta, T.; Kitagawa, T.; Soulimane, T.; Pinakoulaki, E. The structure of the hyponitrite species in a heme Fe-Cu binuclear center. *Angew. Chem., Int. Ed.* **2007**, *46*, 2210-2214.
22. Wijeratne, G. B.; Hematian, S.; Siegler, M. A.; Karlin, K. D. Copper(I)/$NO_{(g)}$ Reductive Coupling Producing a trans-Hyponitrite Bridged Dicopper(II) Complex: Redox Reversal Giving Copper(I)/$NO_{(g)}$ Disproportionation. *J. Am. Chem. Soc.* **2017**, *139*, 13276-13279.
23. Wijeratne, G. B.; Bhadra, M.; Siegler, M. A.; Karlin, K. D. Copper(I) Complex Mediated Nitric Oxide Reductive Coupling: Ligand Hydrogen Bonding Derived Proton Transfer Promotes $N_2O_{(g)}$ Release. *J. Am. Chem. Soc.* **2019**, *141*, 17962-17967.
24. Girsch, P.; de Vries, S. Purification and initial kinetic and spectroscopic characterization of NO reductase from Paracoccus denitrificans. *Biochim. Biophys. Acta* **1997**, *1318*, 202-216.
25. Moënne-Loccoz, P.; de Vries, S. Structural characterization of the catalytic high-spin heme b of nitric oxide reductase: A resonance Raman study. *J. Am. Chem. Soc.* **1998**, *120*, 5147-5152.
26. Brozek, C. K.; Miller, J. T.; Stoian, S. A.; Dincă, M. NO Disproportionation at a Mononuclear Site-Isolated Fe^{2+} Center in Fe^{2+}-MOE-5. *J. Am. Chem. Soc.* **2015**, *137*, 7495-7501.
27. Poskrebyshev, G. A.; Shafirovich, V.; Lymar, S. V. Hyponitrite radical, a stable adduct of nitric oxide and nitroxyl. *J. Am. Chem. Soc.* **2004**, *126*, 891-899.
28. Ohta, T.; Soulimane, T.; Kitagawa, T.; Varotsis, C. Nitric oxide activation by caa_3 oxidoreductase from *Thermus thermophilus*. *Phys. Chem. Chem. Phys.* **2015**, *17*, 10894-10898.
29. Arikawa, Y.; Asayama, T.; Moriguchi, Y.; Agari, S.; Onishi, M. Reversible N-N coupling of NO Ligands on dinuclear ruthenium complexes and subsequent N_2O

evolution: Relevance to nitric oxide reductase. *J. Am. Chem. Soc.* **2007**, *129*, 14160-14161.

30. Caranto, J. D.; Weitz, A.; Hendrich, M. P.; Kurtz, D. M., Jr. The Nitric Oxide Reductase Mechanism of a Flavo-Diiron Protein: Identification of Active-Site Intermediates and Products. *J. Am. Chem. Soc.* **2014**, *136*, 7981-7992.
31. Yi, J.; Morrow, B. H.; Campbell, A. L. O. C.; Shen, J. K.; Richter-Addo, G. B. Nitric oxide coupling mediated by iron porphyrins: the N-N bond formation step is facilitated by electrons and a proton. *Chem. Commun.* **2012**, *48*, 9041-9043.
32. Blomberg, M. R. A. Can Reduction of NO to N_2O in Cytochrome c Dependent Nitric Oxide Reductase Proceed through a Trans-Mechanism? *Biochemistry* **2017**, *56*, 120-131.
33. Berto, T. C.; Speelman, A. L.; Zheng, S.; Lehnert, N. Mono- and dinuclear non-heme iron-nitrosyl complexes: Models for key intermediates in bacterial nitric oxide reductases. *Coord. Chem. Rev.* **2013**, *257*, 244-259.
34. Chakraborty, S.; Reed, J.; Ross, M.; Nilges, M. J.; Petrik, I. D.; Ghosh, S.; Hammes-Schiffer, S.; Sage, J. T.; Zhang, Y.; Schulz, C. E.; Lu, Y. Spectroscopic and Computational Study of a Nonheme Iron Nitrosyl Center in a Biosynthetic Model of Nitric Oxide Reductase. *Angew. Chem., Int. Ed.* **2014**, *53*, 2417-2421.
35. Sabuncu, S.; Reed, J. H.; Lu, Y.; Moënne-Loccoz, P. Nitric Oxide Reductase Activity in Heme-Nonheme Binuclear Engineered Myoglobins through a One-Electron Reduction Cycle. *J. Am. Chem. Soc.* **2018**, *140*, 17389-17393.
36. Kakishima, K.; Shiratsuchi, A.; Taoka, A.; Nakanishi, Y.; Fukumori, Y. Participation of nitric oxide reductase in survival of *Pseudomonas aeruginosa* in LPS-activated macrophages. *Biochem. Biophys. Res. Commun.* **2007**, *355*, 587-591.
37. Justino, M. C.; Ecobichon, C.; Fernandes, A. F.; Boneca, I. G.; Saraiva, L. M. *Helicobacter pylori* Has an Unprecedented Nitric Oxide Detoxifying System. *Antioxid. Redox Signal.* **2012**, *17*, 1190-1200.
38. Flint, A.; Stintzi, A.; Saraiva, L. M. Oxidative and nitrosative stress defences of *Helicobacter* and *Campylobacter* species that counteract mammalian immunity. *FEMS Microbiol. Rev.* **2016**, *40*, 938-960.
39. Gobert, A. P.; Wilson, K. T. The Immune Battle against *Helicobacter pylori*

Infection: NO Offense. *Trends Microbiol.* **2016**, *24*, 366-376.

40. Vázquez-Torres, A.; Bäumler, A. J. Nitrate, nitrite and nitric oxide reductases: from the last universal common ancestor to modern bacterial pathogens. *Curr. Opin. Microbiol.* **2016**, *29*, 1-8.
41. Ravishankara, A. R.; Daniel, J. S.; Portmann, R. W. Nitrous oxide (N_2O): the dominant ozone-depleting substance emitted in the 21st century. *Science* **2009**, *326*, 123-125.
42. de Richter, R.; Caillol, S. Fighting global warming: The potential of photocatalysis against CO_2, CH_4, N_2O, CFCs, tropospheric O_3, BC and other major contributors to climate change. *J. Photochem. Photobiol., C* **2011**, *12*, 1-19.
43. Tolman, W. B. A model for the substrate adduct of copper nitrite reductase and its conversion to a novel tetrahedral copper(II) triflate complex. *Inorg. Chem.* **1991**, *30*, 4877-4880.
44. Ruggiero, C. E.; Carrier, S. M.; Antholine, W. E.; Whittaker, J. W.; Cramer, C. J.; Tolman, W. B. Synthesis and structural and spectroscopic characterization of mononuclear copper nitrosyl complexes: models for nitric oxide adducts of copper proteins and copper-exchanged zeolites. *J. Am. Chem. Soc.* **1993**, *115*, 11285-11298.
45. Ruggiero, C. E.; Carrier, S. M.; Tolman, W. B. Reductive disproportionation of NO mediated by copper complexes: modeling N_2O generation by copper proteins and heterogeneous catalysts. *Angew. Chem., Int. Ed.* **1994**, *33*, 895-897.
46. Schneider, J. L.; Carrier, S. M.; Ruggiero, C. E.; Young, V. G., Jr.; Tolman, W. B. Influences of ligand environment on the spectroscopic properties and disproportionation reactivity of copper-nitrosyl complexes. *J. Am. Chem. Soc.* **1998**, *120*, 11408-11418.
47. Kim, S.; Siegler, M. A.; Karlin, K. D. Peroxynitrite chemistry derived from nitric oxide reaction with a Cu(II)-OOH species and a copper mediated NO reductive coupling reaction. *Chem. Commun.* **2014**, *50*, 2844-2846.
48. Paul, P. P.; Karlin, K. D. Functional modeling of copper nitrite reductases: reactions of NO_2^- or nitric oxide with copper(I) complexes. *J. Am. Chem. Soc.* **1991**, *113*, 6331-6332.
49. Tao, W.; Bower, J. K.; Moore, C. E.; Zhang, S. Dicopper μ-Oxo, μ-Nitrosyl

Complex from the Activation of NO or Nitrite at a Dicopper Center. *J. Am. Chem. Soc.* **2019**, *141*, 10159-10164.

50. Metz, S. N_2O Formation via Reductive Disproportionation of NO by Mononuclear Copper Complexes: A Mechanistic DFT Study *Inorg. Chem.* **2017**, *56*, 3820-3833.
51. (a) Becke, A. D. Density-functional exchange-energy approximation with correct asymptotic behavior. *Phys. Rev. A* **1988**, *38*, 3098-3100. (b) Lee, C.; Yang, W.; Parr, R. G. Development of the Colle-Salvetti correlation-energy formula into a functional of the electron density. *Phys. Rev. B: Condens. Matter Mater. Phys.* **1988**, *37*, 785-789. (c) Becke, A. D. Density-functional thermochemistry. III. The role of exact exchange. *J. Chem. Phys.* **1993**, *98*, 5648-5652.
52. Gaussian 16, Revision A.03, Frisch, M. J.; Trucks, G. W.; Schlegel, H. B.; Scuseria, G. E.; Robb, M. A.; Cheeseman, J. R.; Scalmani, G.; Barone, V.; Petersson, G. A.; Nakatsuji, H.; Li, X.; Caricato, M.; Marenich, A. V.; Bloino, J.; Janesko, B. G.; Gomperts, R.; Mennucci, B.; Hratchian, H. P.; Ortiz, J. V.; Izmaylov, A. F.; Sonnenberg, J. L.; Williams-Young, D.; Ding, F.; Lipparini, F.; Egidi, F.; Goings, J.; Peng, B.; Petrone, A.; Henderson, T.; Ranasinghe, D.; Zakrzewski, V. G.; Gao, J.; Rega, N.; Zheng, G.; Liang, W.; Hada, M.; Ehara, M.; Toyota, K.; Fukuda, R.; Hasegawa, J.; Ishida, M.; Nakajima, T.; Honda, Y.; Kitao, O.; Nakai, H.; Vreven, T.; Throssell, K.; Montgomery, J. A., Jr.; Peralta, J. E.; Ogliaro, F.; Bearpark, M. J.; Heyd, J. J.; Brothers, E. N.; Kudin, K. N.; Staroverov, V. N.; Keith, T. A.; Kobayashi, R.; Normand, J.; Raghavachari, K.; Rendell, A. P.; Burant, J. C.; Iyengar, S. S.; Tomasi, J.; Cossi, M.; Millam, J. M.; Klene, M.; Adamo, C.; Cammi, R.; Ochterski, J. W.; Martin, R. L.; Morokuma, K.; Farkas, O.; Foresman, J. B.; Fox, D. J. Gaussian, Inc., Wallingford CT, 2016.
53. (a) Wachters, A. J. H. Gaussian basis set for molecular wavefunctions containing third-row atoms. *J. Chem. Phys.* **1970**, *52*, 1033-1036. (b) Hay, P. J. Gaussian basis sets for molecular calculations – representation of 3D orbitals in transition-metal atoms. *J. Chem. Phys.* **1977**, *66* 4377-4384. (c) Raghavachari, K.; Trucks, G. W. Highly correlated systems: Excitation energies of first row transition metals Sc-Cu. *J. Chem. Phys.* **1989**, *91*, 1062-1065.
54. Dunning, T. H.; Hay, P. J. Gaussian Basis Sets for Molecular Calculations. in

Modern Theoretical Chemistry, ed. Schaefer, H. F., III, Plenum: New York, 1976; Vol. 3, pp 1-27.

55. (a) Schwabe, T.; Grimme, S. Double-hybrid density functionals with long-range dispersion corrections: higher accuracy and extended applicability. *Phys. Chem. Chem. Phys.* **2007**, *9*, 3397-3406. (b) Grimme, S.; Antony, J.; Ehrlich, S.; Krieg, H. A consistent and accurate ab initio parametrization of density functional dispersion correction (DFT-D) for the 94 elements H-Pu. *J. Chem. Phys.* **2010**, *132*, 154104-154119.
56. Tomasi, J.; Mennucci, B.; Cammi, R. Quantum mechanical continuum solvation models. *Chem. Rev.* **2005**, *105*, 2999-3093.
57. Van Stappen, C.; Lehnert, N. Mechanism of N–N Bond Formation by Transition Metal–Nitrosyl Complexes: Modeling Flavodiiron Nitric Oxide Reductases. *Inorg. Chem.* **2018**, *57*, 4252-4269.

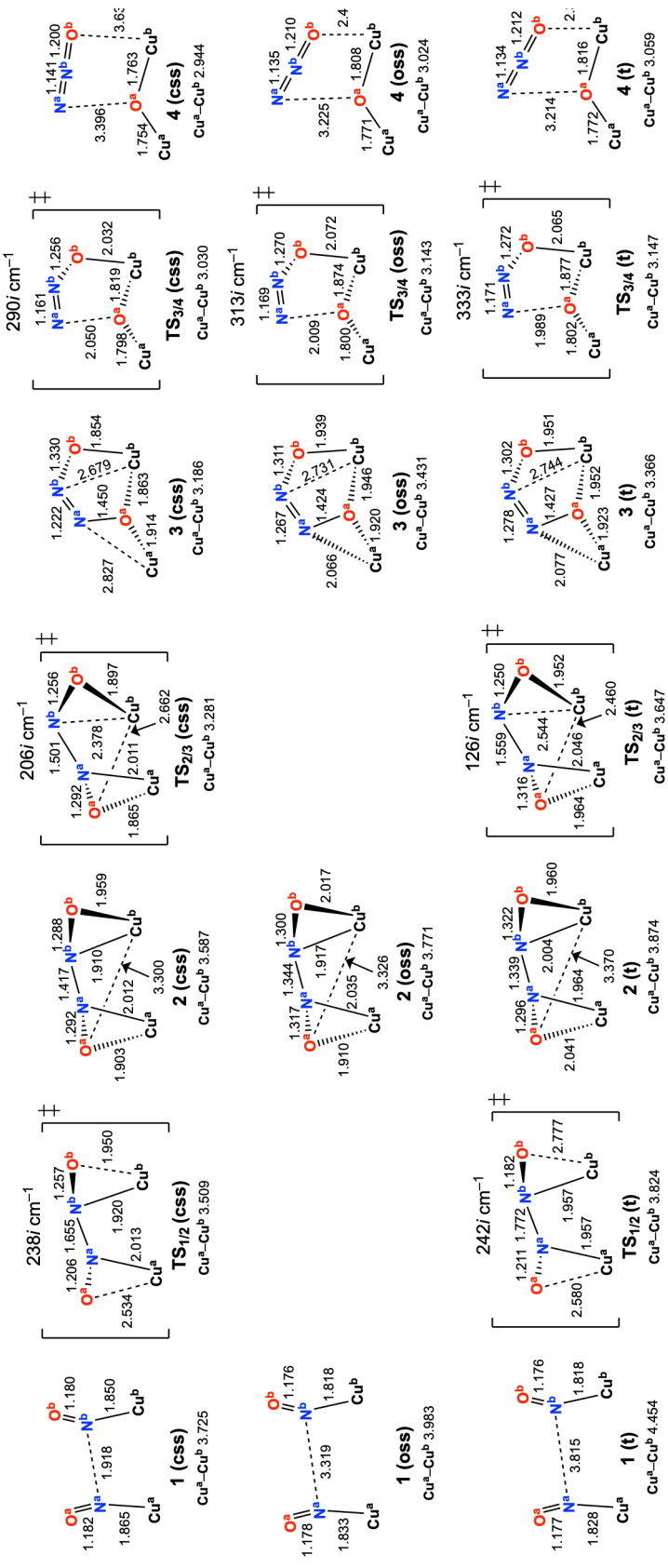

Figure S2-1. Optimized structures of all intermediates in the closed-shell singlet, open-shell singlet and triplet states. Distances are given in a unit of Å.

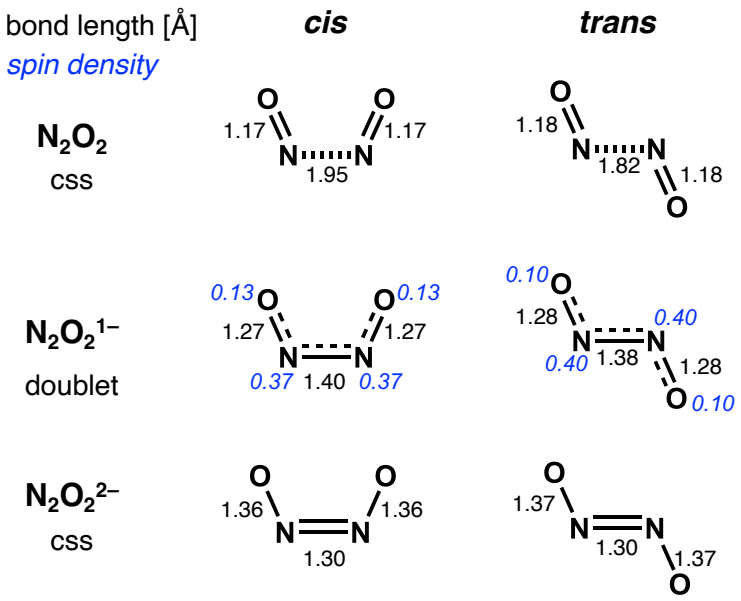

Figure S2-2. Optimized structures of neutral-, mono-anion- and di-anion N_2O_2 species.

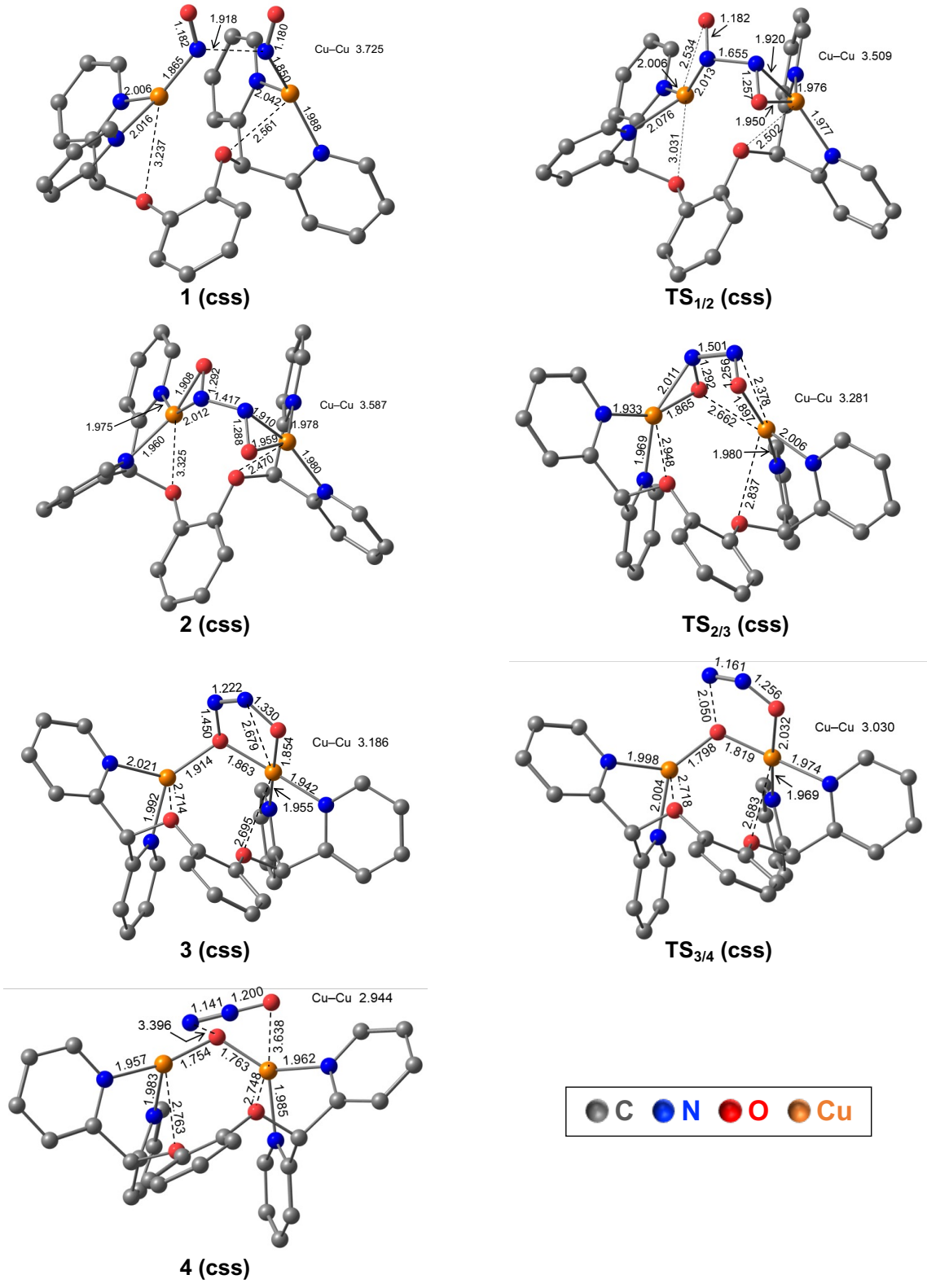

Figure S2-2. Overall structures of all species in the closed-shell singlet (css) state. H atoms are omitted for clarity. Bond distances are given in a unit of Å.

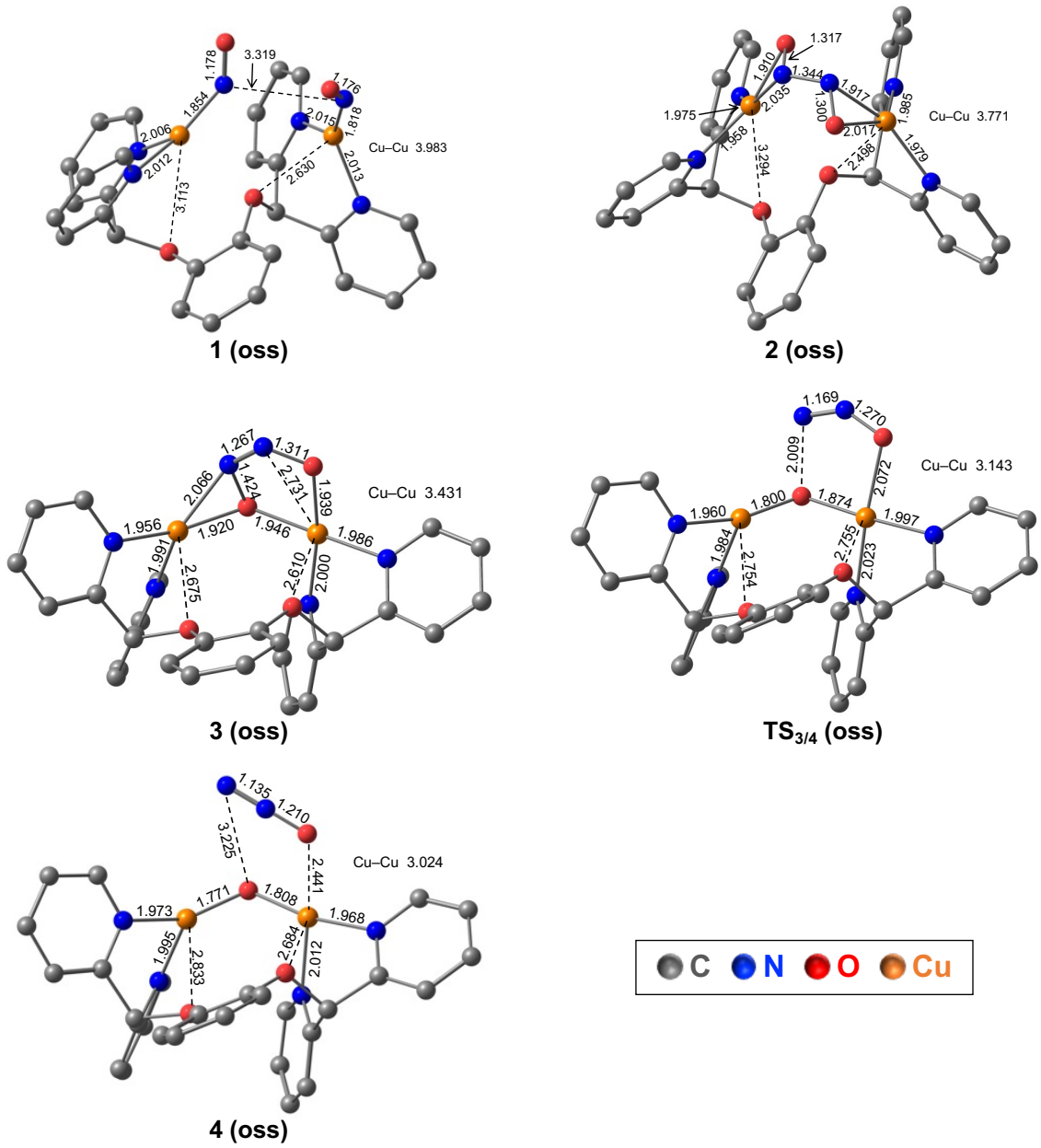

Figure S2-3. Overall structures of all species in the open-shell singlet (oss) state. H atoms are omitted for clarity. Bond distances are given in a unit of Å.

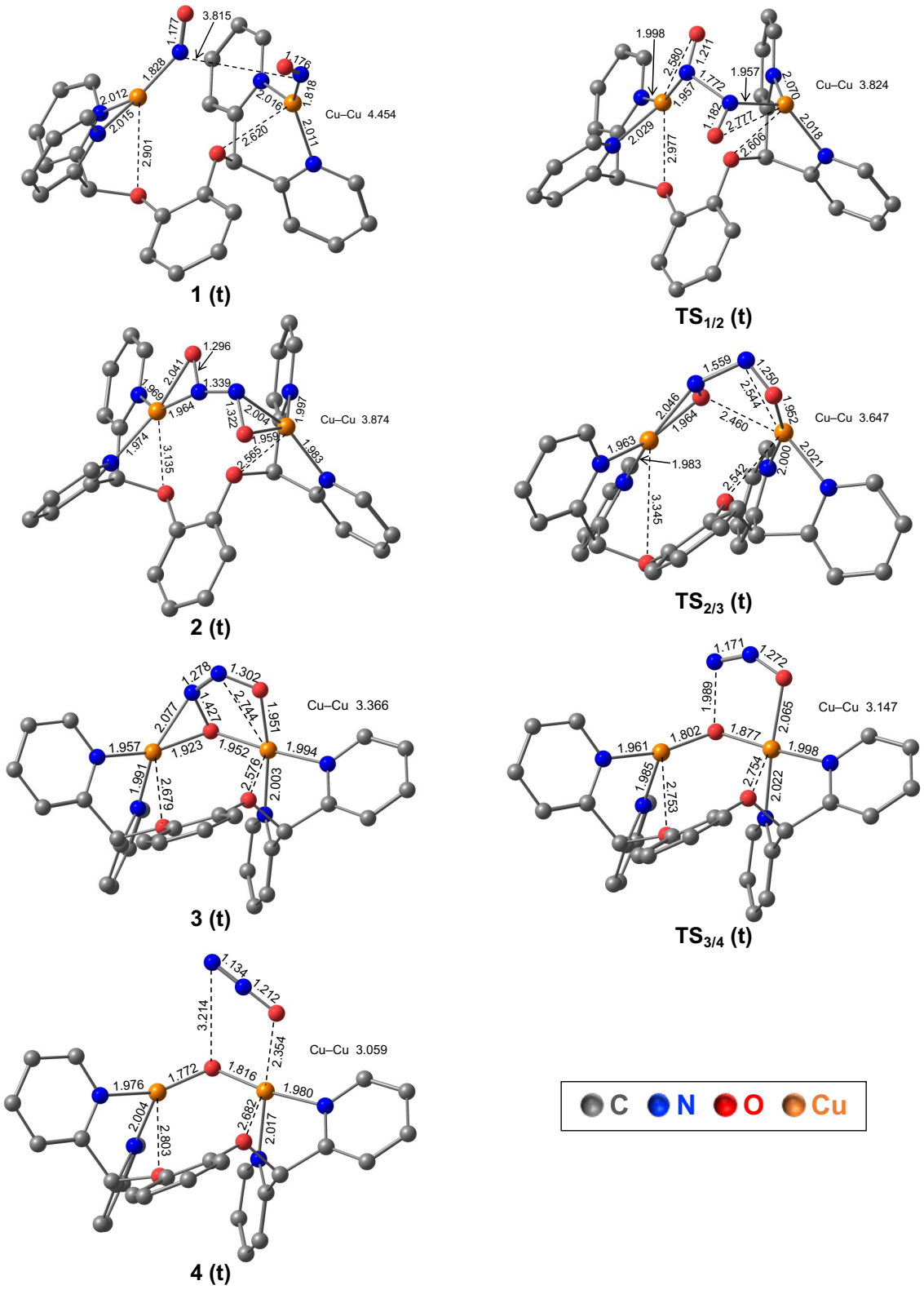

Figure S2-4. Overall structures of all species in the triplet (t) state. H atoms are omitted for clarity. Bond distances are given in a unit of Å.

Table S2-1. Calculated Mulliken charges of all intermediates.

Closed-shell singlet

	1	**$TS_{1/2}$**	**2**	**$TS_{2/3}$**	**3**	**$TS_{3/4}$**	**4**
Cu^a	0.33	0.31	0.33	0.32	0.43	0.44	0.41
Cu^b	0.28	0.24	0.25	0.32	0.38	0.36	0.48
N^a	0.09	0.11	0.12	0.08	0.11	0.04	-0.08
N^b	0.09	0.08	0.13	0.11	0.11	0.29	0.35
O^a	-0.07	-0.09	-0.24	-0.21	-0.46	-0.57	-0.54
O^b	-0.07	-0.17	-0.24	-0.17	-0.29	-0.22	-0.21

Open-shell singlet

	1	**$TS_{1/2}$**	**2**	**$TS_{2/3}$**	**3**	**$TS_{3/4}$**	**4**
Cu^a	0.31	-	0.34	-	0.44	0.51	0.45
Cu^b	0.30	-	0.29	-	0.39	0.38	0.41
N^a	0.05	-	0.13	-	0.07	0.04	-0.08
N^b	0.06	-	0.14	-	0.07	0.24	0.40
O^a	-0.04	-	-0.30	-	-0.40	-0.60	-0.60
O^b	-0.03	-	-0.28	-	-0.32	-0.28	-0.21

Triplet

	1	**$TS_{1/2}$**	**2**	**$TS_{2/3}$**	**3**	**$TS_{3/4}$**	**4**
Cu^a	0.32	0.35	0.41	0.41	0.44	0.51	0.45
Cu^b	0.30	0.35	0.26	0.35	0.40	0.38	0.41
N^a	0.06	0.02	0.26	0.05	0.05	0.04	-0.07
N^b	0.06	0.09	0.00	0.07	0.08	0.24	0.40
O^a	-0.04	-0.10	-0.25	-0.27	-0.40	-0.58	-0.59
O^b	-0.03	-0.04	-0.31	-0.17	-0.30	-0.28	-0.21

Table S2-2. Calculated Mulliken spin densities of all intermediates.

Open-shell singlet

	1	**$TS_{1/2}$**	**2**	**$TS_{2/3}$**	**3**	**$TS_{3/4}$**	**4**
Cu^a	0.01	-	0.37	-	0.53	0.62	0.51
Cu^b	-0.01	-	-0.34	-	-0.57	-0.56	-0.61
N^a	0.60	-	-0.17	-	0.02	0.02	-0.02
N^b	-0.61	-	0.11	-	0.03	0.03	0.01
O^a	0.38	-	0.00	-	0.03	-0.05	0.16
O^b	-0.38	-	0.03	-	-0.05	-0.08	-0.01

Triplet

	1	**$TS_{1/2}$**	**2**	**$TS_{2/3}$**	**3**	**$TS_{3/4}$**	**4**
Cu^a	0.01	0.26	0.48	0.45	0.53	0.62	0.50
Cu^b	0.01	0.06	0.38	-0.32	0.59	0.56	0.59
N^a	0.62	0.45	0.40	0.77	0.00	-0.05	0.02
N^b	0.61	0.29	-0.10	0.49	0.09	0.01	-0.01
O^a	0.38	0.51	0.44	0.44	0.20	0.39	0.55
O^b	0.38	0.34	0.10	0.11	0.20	0.09	0.02

Chapter 3. Mechanistic Study of Reduction of Nitrite to NO by the Copper(II) Complex: Different Concerted Proton–Electron Transfer Reactivity between Nitrite and Nitro Complexes

3.1. Introduction

The reduction of nitrite (NO_2^-) to nitric oxide (NO) has attracted intensive attention because of its critical roles in the biogeochemical nitrogen cycle and numerous physiological processes. In a denitrification process of the nitrogen cycle, nitrate (NO_3^-) and NO_2^- are sequentially converted into N_2 ($NO_3^- \rightarrow NO_2^- \rightarrow NO \rightarrow N_2O \rightarrow N_2$) by different microbial metalloenzymes.[1–5] The reduction of NO_2^- to NO is the second step of the denitrification and is catalyzed by nitrite reductases (NiRs) such as Cu-containing NiR and heme-containing NiR.[3–11] The physiological role of NO_2^- reduction is the synthesis of NO, which functions as a signaling agent during immune response, vasodilation, and neurotransmission, among other functions.[12,13] Such NO_2^- reduction as a NO reservoir is performed by Mo-containing NiRs such as xanthine oxidase, aldehyde oxidase, sulfite oxidase and mainly by globins.[6,14–18]

Several studies on the reduction of NO_2^- by Cu complexes have been reported. Spectroscopic studies and X-ray crystal structure determinations have revealed important aspects of NO_2^- reduction at Cu active centers.[19–32] Woollard-Shore et al. reported the synthesis, characterization, and catalytic properties of four Cu(II) complexes as catalytic agents for NO_2^- reduction.[20] Their crystallographic study revealed three different coordination modes: η^1-NO_2, η^1-ONO, and η^2-ONO. Hunt et al. investigated electrocatalytic activities for nitrite reduction using six Cu(II) complexes and showed the relationship between the reactivity and electrochemical properties.[26] Maji et al. conducted an electrochemical study and suggested that the coordination mode is isomerized from η^2-ONO to η^1-NO_2 during NO_2^- reduction by a Cu(II) complex.[30] Computational studies have also provided beneficial information. Geometry optimization using density functional theory (DFT) calculations has been used to compare the deduced structures with experimentally obtained structures, and molecular orbital analysis has been used to clarify the corresponding electronic structures.[33–36] Symes and coworkers carried out a

calculation for the formation of Cu(II)–HNO_2 from Cu(II)–NO_2 and the corresponding transition state of proton transfer from ligand-derived phenol to NO_2^-, where the activation energy was calculated to be 33.5 kcal/mol.[35] Szymczak and coworkers carried out a calculation for the reaction from Cu(I)–NO_2 to Cu(II)–OH and a corresponding transition state with an activation energy of 21.7 kcal/mol.[36] Thus, the reaction mechanism for Cu-mediated NO_2^- reduction has been investigated using both experimental and theoretical methods. In addition, the involvement of concerted proton–electron transfer (CPET) has been proposed on the basis of kinetic isotope effect studies.[35] However, detailed information, such as the source of the protons and electrons and the mechanism by which NO is released, is lacking.

This work aims to highlight the mechanistic features of NO_2^- reduction by a Cu(II) complex, as described by Kundu and coworkers.[37] They reported the phenol-mediated reduction of NO_2^- to NO by a Cu(II) complex supported by a tripodal-heteroditopic-cryptand ligand (**L**) (Figure 3-1). The reaction of 2,4-di-*tert*-butylphenol with the nitrite copper(II) complex ($[Cu^{II}(\mathbf{L})(ONO)]^+$) forms the hydroxyl copper(II) complex ($[Cu^{II}(\mathbf{L})(OH)]^+$), NO, and 3,3′,5,5′-tetra-*tert*-butyl-(1,1′-biphenyl)-2,2′-diol (biphenol). The biphenol was presumed to be formed by coupling of the corresponding phenoxyl radical (Figure 3-1). Corresponding mechanistic studies indicated the involvement of concerted proton-electron transfer (CPET) in the NO_2^- reduction. In the present study, we carried out the density functional theory (DFT) calculations to elucidate the reaction

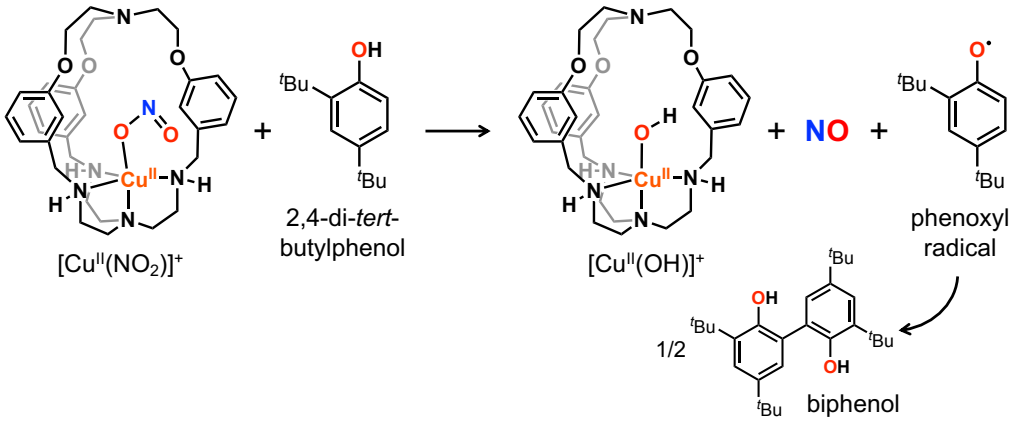

Figure 3-1. Reaction scheme of the nitrite reduction reported in ref 37.

pathway for NO_2^- reduction. We focused on a change in the electronic structure during the conversion from NO_2^- into NO by the Cu(II) complex. On the basis of DFT calculations conducted using intrinsic reaction coordinate (IRC) and intrinsic bond orbital (IBO) analyses, we deduced a reaction mechanism for the reduction of NO_2^- and successfully described the precise CPET behavior. The results of our IRC and IBO analyses demonstrate the importance of asynchronicity between PT and ET in CPET reactions.

3.2. Computational Methods

We investigated the mechanism for NO_2^- reduction by a Cu(II) complex using DFT calculations. We used the B3LYP method,[38–40] which has been widely used for simulating various transition-metal complexes for more than 25 years. All calculations were performed using spin-unrestricted DFT implemented in the Gaussian 16 package[41] for the structural optimization. The spin densities were calculated by the Mulliken population analysis. Because the total charge of the Cu(II) complex is +1, we considered the doublet state. Vibration frequencies were systematically computed to ensure that the potential-energy surface associated with each optimized geometry corresponded to a local minimum with no imaginary frequencies, or to a saddle point with only one imaginary frequency. We used the 15s11p6d primitive set of Wachters−Hay supplemented with one polarization f-function (α = 1.44 for Cu)[42–44] for the Cu atoms and the 6-31G** basis set[45–47] for the H, C, N, and O atoms. We added Grimme's dispersion correction (D3).[48,49] The B3LYP-D3 method provides good results for the calculation of copper complex, as does the coupled cluster method.[50] Implicit solvent effects of acetonitrile (ε = 35.688) were included via the polarizable continuum model (PCM).[51] Intrinsic reaction coordinate (IRC) analysis was conducted to confirm transition states and to follow the change of electronic structures in the vicinity of transition states.[52,53] Using the IRC method, we can also trace the steepest descent path from the transition state. The reaction coordinate (s) in the N-atoms system is defined as follows:

$$ds^2 = \sum_{i=1}^{3N} \left(\sqrt{m_i} dx_i\right)^2$$

where x_i and m_i are the cartesian coordinates and the atomic mass of the atom i, respectively. Since ***ds*** is defined as the sum of the displacements of each moving atom corresponding to molecular deformation, it is used as a quantitative measure of molecular deformation. To characterize a concerted reaction which contains multiple chemical events, the IBO method was used.[54–56] To calculate IBOs, we carried out single-point calculations at the B3LYP/def2-TZVP level[57,58] of theory using TURBOMOLE rev. V7.5.0,[59] where the transition state and the IRC structures were obtained using the Gaussian 16 program. IBOs are generated and visualized by IboView[54] using electron structure data calculated by TURBOMOLE.

3.3. Results and Discussion

Optimized Structures of $CuNO_2$ Complexes

We first consider the initial complex $[LCu^{II}ONO]^+$ in the NO_2^- reduction by Cu(II), where L is a tripodal-heteroditopic-cryptand ligand. Figure 3-2 shows the X-ray crystal structure and the two DFT-optimized structures. DFT calculations suggested two coordination modes: an O-coordinated Cu(II)–nitrite complex (**IC*O***), and an N-coordinated Cu(II)–nitro complex (**IC*N***). These two coordination modes have been reported in both experimental[20,23,33] and computational studies.[30,33] For the X-ray crystal structure in Figure 3-2(a), the N1–O1 bond length, the N1–O2 bond length, and the O1–N1–O2 bond angle are 1.280(2) Å, 1.230(2) Å, and 114.01(14)°, respectively, which are completely consistent with **IC*O*** (the values are 1.290 Å, 1.234 Å, and 116°, respectively) in Figure 3-2(b). Both the X-ray crystal structures and the **IC*O*** show the η^1-O1 binding mode for NO_2^-. In the two structures, no significant difference is observed in the Cu–O1 and Cu–O2 distances. Additionally, the calculated spin density of Cu (0.56) and optimized structure indicate **IC*O*** has the d^9 Cu^{II} state with a distorted octahedral structure, which is consistent with the X-band electron paramagnetic resonance (EPR) spectrum reported by Kundu et al.[37] These computed results indicate that our model and method are sufficient to correctly represent the chemistry of the active site of the Cu(II) complex supported by a tripodal-heteroditopic-cryptand ligand.

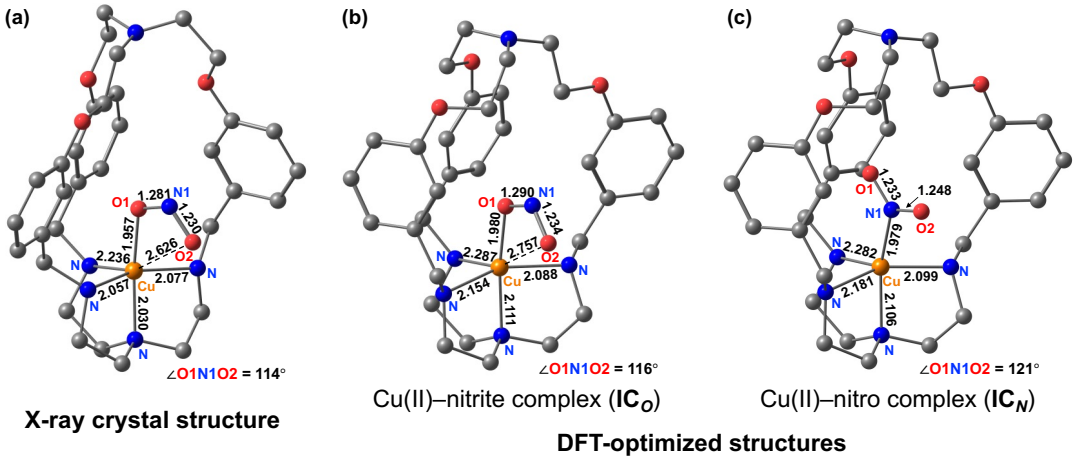

Figure 3-2. X-ray crystal structure reported in Ref. 37 (a) and DFT-optimized structures of O-coordinated Cu(II)–nitrite complex (**IC*O***) (b) and N-coordinated Cu(II)–nitro complex (**IC*N***) (c). Bond distances are expressed in Å. H atoms are omitted for clarity.

The DFT calculations suggest another stable structure, **IC*N*** (Figure 3-2(c)), which differs from the X-ray crystal structure. Because **IC*N*** is 3.8 kcal/mol higher in the free energy than **IC*O***, only O-coordinated species can be obtained from the X-ray crystal structure. The calculations show that one structure is experimentally confirmed and the other is a new structure. Thus, two initial complexes—**IC*O*** and **IC*N***—are considered; no significant geometrical difference exists between them except for the coordination modes of the NO_2 ligand.

Two Reaction Pathways

The DFT calculations suggest the two initial complexes, **IC*O*** and **IC*N***. Therefore, two reaction pathways from **IC*O*** (nitrite pathway) and **IC*N*** (nitro pathway) were examined. Both reaction pathways finally lead to the same product—$[Cu(II)OH]^+$, NO, and ArO$^\bullet$—(**FC**). In the nitrite pathway (Figure 3-3), the reaction of **IC*O*** with ArOH forms the reactant complex **RC*O***. In **RC*O***, the O1–H1 distance was calculated to be 1.794 Å, indicating the formation of a hydrogen bond. Such an interaction provides an asymmetrical structure of the ONO moiety because of elongation of the O1–N1 bond, where the distances were calculated to be 1.290 Å in **IC*O*** and 1.313 Å in **RC*O***. The H atom migration and the O1–N1 bond cleavage simultaneously proceed through transition state **TS*O*** with an activation energy of 25.2 kcal/mol. The O1–N1 bond is elongated from 1.313 Å in **RC*O*** to 1.817 Å in **TS*O***, whereas the N1–O2 bond is shortened from 1.220 Å in **RC*O*** to 1.166 Å in **TS*O***, indicating that the N1–O2 moiety is ready to be released as an NO molecule. The β-spin density on the N1 and O2 atoms increases from 0.02 and 0.01 in **RC*O*** to –0.36 and –0.19 in **TS*O***, respectively, indicating impending formation of NO. Similarly, the α-spin density for the O3 atom increases from 0.00 in **RC*O*** to 0.22 in **TS*O***, indicating that the system is approaching the formation of ArO$^\bullet$. After **TS*O***, the Cu(II)OH complex, ArO$^\bullet$, and NO (**PC*O***) are present. In **PC*O***, the O3–H1 distance was calculated to be 1.970 Å, where ArO$^\bullet$ is attracted by the hydrogen bond between the O3 atom and H1 atom. The O1–N1 distance further increases to 2.387 Å. The spin densities for the Cu, N1, O1, O2, and O3 in **PC*O*** were calculated to be 0.58, –0.69, 0.17, –0.31, and 0.34, respectively (Table 3-1). Although the spin density for the Cu(II) center remains unchanged, the reaction is observed to increase the α-spin density for ArO$^\bullet$ and the β-spin

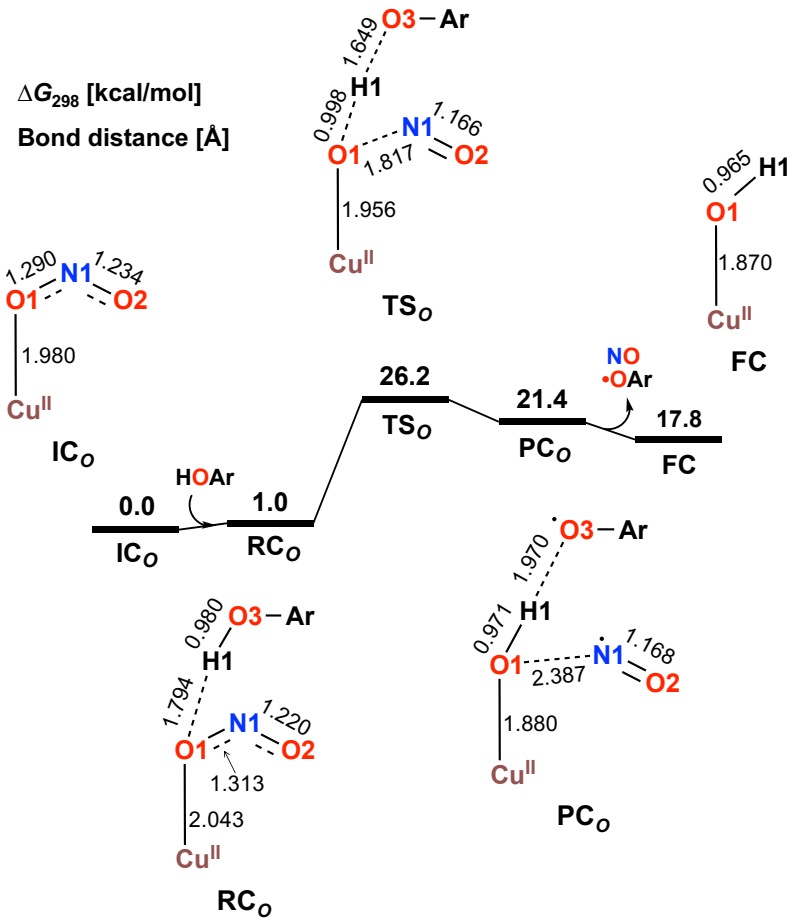

Figure 3-3. Computed free energy diagram for the nitrite pathway and optimized geometries of Cu active site for reactant complex (**RC***o*), transition state (**TS***o*), and product complex (**PC***o*). **IC** and **FC** indicate an initial complex and a final complex.

Table 3-1. Calculated Mulliken spin densities for reaction species along the nitrite pathway.

	Cu	N1	O1	O2	O3	ArO
IC*o*	0.56	0.02	0.11	0.00	-	-
RC*o*	0.56	0.02	0.08	0.01	0.00	0.00
TS*o*	0.54	–0.36	0.12	–0.19	0.22	0.61
PC*o*	0.58	–0.69	0.17	–0.31	0.34	1.00
FC	0.59	-	0.16	-	-	-

density for NO because of spin polarization within the complex. Given the changes in geometry and spin density, two events proceed in concert in this step: electron transfer (ET) from ArOH to the N1O2 moiety and proton transfer (PT) from ArOH to the O1 atom. That is, ArOH provides an electron for one and a proton for another. This reaction can be categorized as CPET. At last, **FC**, where NO and ArO$^{\bullet}$ were released, is calculated to be 3.6 kcal/mol lower than **PC*o***. The overall reaction in the nitrite pathway was calculated to be endothermic by 17.8 kcal/mol. When the position of **TS*o*** in the reaction is considered, the transition state is late in molecular structure and early in electronic structure. **TS*o*** is geometrically similar to **PC*o***, indicating that **TS*o*** should be categorized as a late transition state.

Meanwhile, the nitro pathway (Figure 3-4) involves three steps: (1) H-atom migration ($[Cu^{II}NO_2]^+ + ArOH \rightarrow [Cu^{I}(HONO)]^+ + ArO^{\bullet}$), (2) N–O bond cleavage ($[Cu^{I}(HONO)]^+ + ArO^{\bullet} \rightarrow [Cu(OH)(NO)]^+ + ArO^{\bullet}$), and (3) NO desorption ($[Cu(OH)(NO)]^+ + ArO^{\bullet} \rightarrow [Cu^{II}OH]^+ + NO + ArO^{\bullet}$). The reaction begins with the association of $\mathbf{IC}_N$ with ArOH to form the reactant complex $\mathbf{RC}_N$ with a binding energy of 5.1 kcal/mol. In $\mathbf{RC}_N$, the O2–H1 distance was calculated to be 1.840 Å, resulting in the formation of a hydrogen bond.

Then, H atom migration from ArOH to NO_2^- occurs with an activation energy of 22.8 kcal/mol, leading to the HONO intermediate $[Cu(HONO)]^+$ with $ArO^{\bullet}$ ($\mathbf{IM1}_N$). In this reaction, O3–H1 bond cleavage and O2–H1 bond formation occur. The O3–H1 (O2–H1) bond length in the transition state ($\mathbf{TS1}_N$) is calculated to be 1.307 Å (1.140 Å), which is

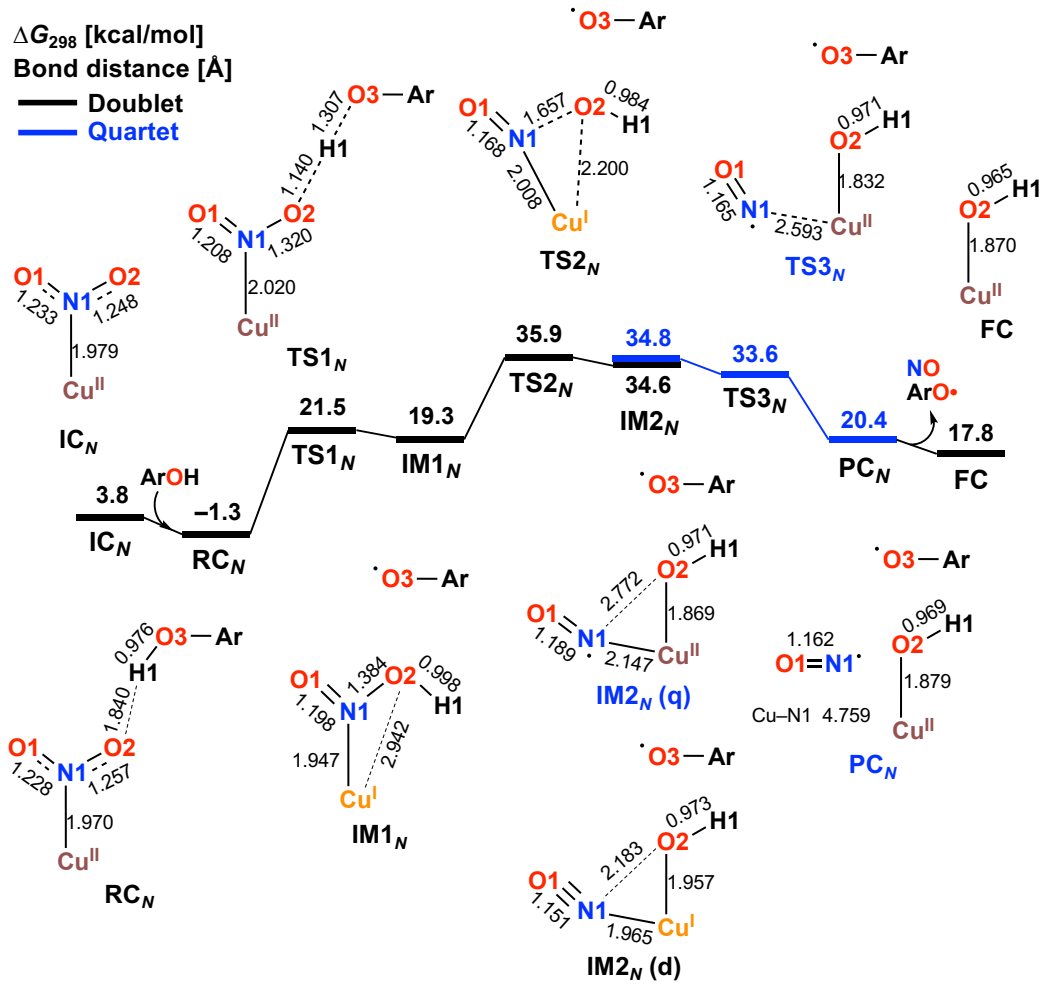

Figure 3-4. Computed free energy diagram for the nitro pathway and optimized geometries of the Cu active site along the reaction. **IM** indicates an intermediate. ΔG are measured from $\mathbf{IC}_O$ in Figure 3-2.

shorter (longer) than that for O3–H1 (O1–H1), indicating that the acceptance of H atoms by the NO_2 moiety is lower in Path 2 than in Path 1. The HONO ligand in **IM1*N*** consists of the N1–O1 bond with a length of 1.198 Å, the N1–O2 bond with a length of 1.384 Å, and the O2–H1 bond with a length of 0.998 Å, structurally corresponding to an isolated HONO molecule (see Figure S3-1). In H-atom migration, additionally, one of the ligand-N–Cu bonds is cleaved (Figure S3-3), where the ligand-N–Cu length increases from 2.178 Å in **RC*N*** to 3.190 Å in **IM1*N*** via 3.122 Å in **TS1*N***, resulting in the four-coordinated Cu species. As shown in Table 3-2, the spin density for the Cu atom decreases from 0.51 in **RC*N*** to 0.00 in **IM1*N*** via 0.21 in **TS1*N***, whereas that for the O3 atom increases from 0.00 in **RC*N*** to 0.29 in **IM1*N*** via 0.17 in **TS1*N***. The changes in geometry and spin density indicate that two main events are occurring in this step: electron transfer (ET) from ArOH to Cu(II) to form Cu(I), and proton transfer (PT) from ArOH to NO_2^- to form HONO. Therefore, we concluded that the first step in the nitro pathway is a CPET reaction in which ArOH acts as both the electron and proton source.

After the formation of the HONO ligand, the N1–O2 bond cleavage forms the nitrosyl hydroxyl complex $[Cu(NO)(OH)]^+$ (**IM2*N***) having two spin states corresponding to $Cu^{I}NO^+$ (doublet) and $Cu^{II}NO^0$ (quartet). **IM2*N*** in the doublet state (**IM2*N* (d)**) has an

Table 3-2. Calculated Mulliken spin densities for reaction species along the nitro pathway.

	Cu	N1	O1	O2	O3	ArO
IC*N*	0.50	0.12	0.04	0.04	-	-
RC*N*	0.51	0.11	0.03	0.03	0.00	0.00
TS1*N*	0.21	0.01	0.00	0.01	0.17	0.65
IM1*N*	0.00	0.00	0.00	0.00	0.29	0.99
TS2*N*	0.00	0.00	0.00	0.00	0.31	1.00
IM2*N* (d)	0.00	0.00	0.00	0.00	0.33	1.00
IM2*N* (q)	0.56	0.69	0.34	0.19	0.32	0.99
TS3*N*	0.59	0.69	0.31	0.20	0.32	0.99
PC*N*	0.57	0.70	0.29	0.17	0.33	1.00
FC	0.59	-	-	0.16	-	-

N1–O1 bond length of 1.151 Å and a spin density of 0.00 for the Cu, N1, and O atoms, whereas **IM2*N*** in the quartet state (**IM2*N* (q)**) has an N1–O1 bond length of 1.189 Å and spin densities of 0.56, 0.69, and 0.34 for Cu, N1, and O1 atoms, respectively. The ΔG_{298} of **IM2*N*** are calculated to be 34.6 kcal/mol in the doublet state and 34.8 kcal/mol in the quartet state. Thus, the spin inversion of **IM2*N*** from a doublet into a quartet is energetically likely to occur because of the small energy difference.

The final step involves NO ligand dissociation from the Cu center. Whereas the computed activation barrier from **IM2*N* (q)** to **TS3*N*** is 0.4 kcal/mol in electronic energy, this step is calculated to be barrierless in ΔG. The Cu–N1 bond is elongated from 2.147 Å in **IM2*N* (q)** to 4.759 Å in **PC*N*** via 2.593 Å in **TS3*N***. Accompanying the desorption of NO, the ligand-N–Cu distance decreases from 3.371 Å in **IM2*N* (q)** to 2.223 Å in **PC*N*** via 3.242 Å in **TS3*N***, resulting in a five-coordinated Cu complex, where four ligand-N and one hydroxyl bind to the Cu atom (Figure S3-3). This step can also proceed in the broken-symmetry doublet state, which is calculated to be almost identical to the result of quartet state (see Figure S3-4). Finally, the release of NO and ArO$^{\bullet}$ leads to **FC** as well the nitrite pathway. The calculated rate-determining step is H-atom migration with an activation energy of 22.8 kcal/mol. Thus, DFT calculations suggest that the nitrite pathway ($\Delta G^{\ddagger}_{\mathbf{TS}\boldsymbol{O}}$ = 25.2) and the nitro pathway ($\Delta G^{\ddagger}_{\mathbf{TS1}\boldsymbol{N}}$ = 22.8) are comparable. Kundu and coworkers suggested from their kinetic investigation that the rate-determining step involves an electron transfer.[37] Our calculated results also show the rate-determining steps are the CPET reaction, which contains an electron transfer (ET), via **TS*O*** in the nirtrite pathway and via **TS1*N*** in the nitro pathway. The experimental prediction was confirmed by our DFT calculations.

IRC Analysis

The above mentioned approach allowed tracing changes on the potential energy surface by connecting discrete points of stable structures and transition states; however, further insights can be obtained by using the IRC calculations to trace continuous changes in electronic energies, geometries, and electronic configurations, particularly regarding the CPET mechanism. To better understand the CPET-derived NO_2^- reduction, we carefully examined the electronic state changes associated with the structural changes derived from the IRC analysis, revealing the PT and ET behavior along the reaction coordinate. Over the past decade, a mechanism involving the concerted but asynchronous movement of a proton and an electron (i.e., asynchronous CPET) has been proposed.[60–66] Given the existence of multiple CPET mechanisms, a detailed analysis requires information on the sequential changes in charge and structure along the reaction path. To this aim, IRC calculations, which can determine the reaction pathway itself, are highly valuable. Herein, we introduce indices to spotlight the asynchronicity of PT and ET in a CPET reaction, which we called PT point and ET point, respectively. The PT and ET points designate the location of the middle progression of PT and ET in the reaction coordinate as depicted in Figure 3-5. Calculating the gap between PT and ET points allows evaluating quantitatively their asynchronicity. In particular, the PT point is the location where the two O–H bonds are of the same length and the ET point is the location where 50% of the total change in the spin density of the atoms involved in ET occurs. Calculating the gap

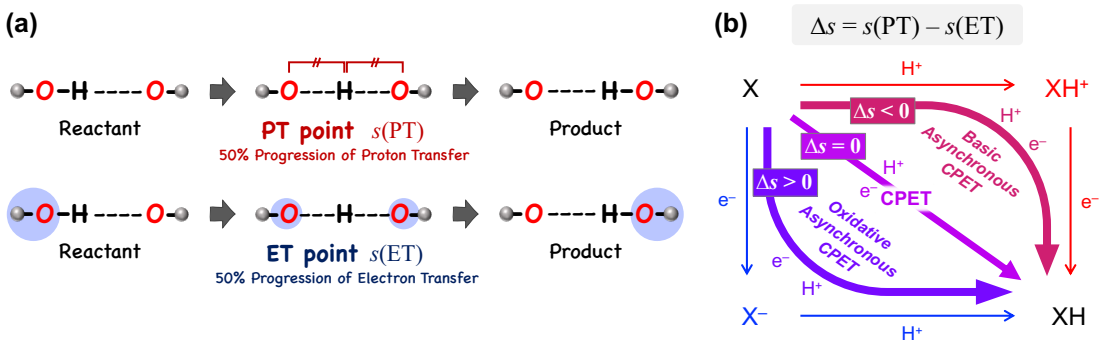

Figure 3-5. (a) Conceptual representation of the definition of proton transfer (PT) point and electron transfer (ET) point. (b) Application of PT and ET points to the square scheme. When $\Delta s < 0$, PT occurs prior to ET (basic-asynchronous CPET). When $\Delta s = 0$, PT and ET proceed simultaneously (synchronous CPET). When $\Delta s > 0$, ET occurs before PT (oxidative-asynchronous CPET).

between PT and ET points (Δs) allows evaluating quantitatively their asynchronicity and classifying the type of CPET (Figure 3-5(b)).

The IRC calculation results shown in Figure 3-6 revealed changes in bond distance and spin density as a function of the reaction coordinate (s), where a reaction coordinate of s = 0.0 corresponds to a transition state. The values of two O–H distances, one N–O distance, and the spin densities for the Cu, N1, O1, O2, and O3 atoms are shown. In the PT point, the two O–H bonds are of equal length, and the O–H distances change before and after PT. Meanwhile, in the ET point, 50% of the total change in spin density for the atoms involved in ET occurs. The results for the reaction from $\mathbf{RC}_{\boldsymbol{O}}$ to $\mathbf{PC}_{\boldsymbol{O}}$ via $\mathbf{TS}_{\boldsymbol{O}}$ in the nitrite pathway are shown in Figures 3-6(a) and 3-6(c). As depicted in Fig. 3-6(a), the increase in the O3–H1 distance and the decrease in the O1–H1 distance, which correspond to the migration of the H1 atom from the O3 atom to the O1 atom, is nearly complete before reaching the transition state (s = 0.0). However, the O1–N1 distance consistently increases throughout the reaction. Here, the PT point is defined as the intersection between the two plots of the O1–H1 and O3–H1 distances, which was determined to be s(PT) = −1.72. Figure 3-6(c) shows that the α-spin emerges on the O3 atom, whereas the β-spin appears on the N1 and O2 atoms. The ET point is defined as the 50% completion point of the spin-density change for the N1 atom, which was identified as s(ET) = −0.07. Consequently, $\Delta s = s(\mathrm{PT}) - s(\mathrm{ET}) = -1.65$, indicating that PT occurs earlier than ET. These computational results indicate that $\mathbf{TS}_{\boldsymbol{O}}$ represents a basic-asynchronous CPET, with "basic" referring to the dominance of the acid–base character.[62,66]

Figures 3-6(b) and 3-6(d) illustrate the results for the reaction from **RC$_N$** to **IM1$_N$** via **TS1$_N$** in nitro pathway. As shown in Figure 3-6(b), the increase in the O3–H1 distance and the decrease in the O2–H1 distance, corresponding to the migration of the H1 atom from the O3 atom to the O2 atom, progress considerably near s = 0. The O1–N1 distance also increases substantially near s = 0; however, this change is minimal and can be attributed to the elongation of the N–O bond from a double bond to a single bond. In this case, the PT point, which is defined as the intersection between the two plots of the O2–

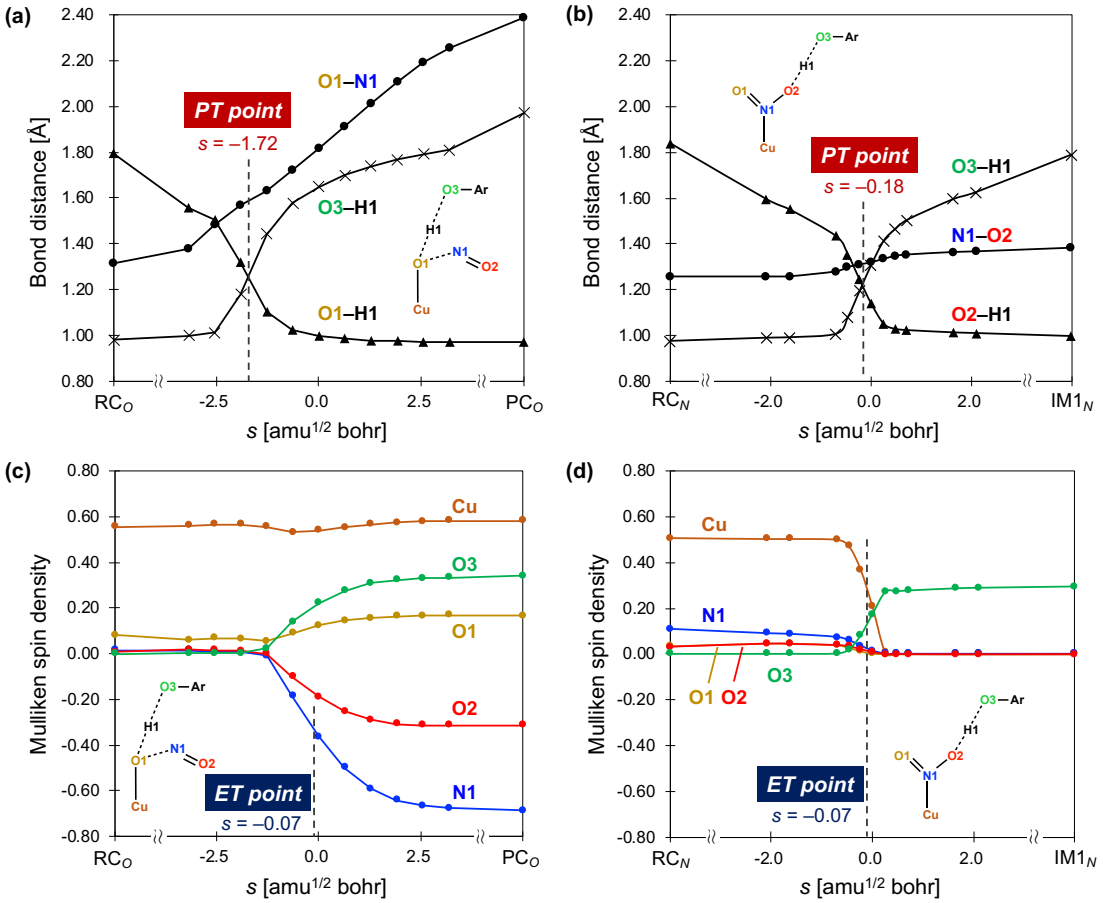

Figure 3-6. Intrinsic reaction coordinate plots of the changes in bond distances and spin densities from **RC$_O$** to **PC$_O$** via **TS$_O$** in the nitrite pathway (a,c) and from **RC$_N$** to **IM1$_N$** via **TS1$_N$** in the nitro pathway (b,d) as a function of the reaction coordinate s [amu$^{1/2}$ bohr]. The transition state lies at s = 0.0. The proton transfer (PT) point is defined as the intersection between the two O–H distances (O1–H1 and O3–H1 in (a) and O2–H1 and O3–H1 in (b)). The electron transfer (ET) point is defined as the point where the spin density for the N1 (Cu) atom reaches the midpoint of **RC$_O$** and **PC$_O$** in (c) (**RC$_N$** and **IM1$_N$** in (d)).

H1 and O3–H1 distances, was determined to be s(PT) = −0.18. Figure 3-6(d) shows an increase and a decrease in the spin densities on the Cu atom and the O3 atom, respectively. The ET point, defined as the 50% completion point of the spin-density change for the Cu atom, was identified as s(ET) = −0.07. Consequently, a gap of Δs = −0.11 exists between PT and ET, indicating that both processes progress almost synchronously. According to the IRC results, the reaction step via **TS1*N*** was classified as a synchronous CPET.

The concept of PT and ET points allows evaluating simple reactions involving the transfer of one proton and one electron. However, it is expected to be applicable to the elucidation of more complex reaction mechanisms in biological systems, such as ion channels, which involve the transfer of multiple protons and electrons.

IBO Analysis

The IRC analysis showed that the nitrite pathway proceeds via *asynchronous* CPET. Here, to determine how the asynchronicity arises in the NO_2^- reduction of the nitrite pathway, we performed an IBO analysis, as developed by Knizia and coworkers.[54] The common Kohn-Sham molecular orbital is often delocalized in the case of transition-metal complexes, which makes tracking the change of an orbital on a certain moiety along the reaction coordinate difficult. By contrast, IBO is suitable for clearly representing the change in electronic structure along the reaction coordinate. The IBO analysis is an appropriate method to represent electron flow through transition states, distinguish between classes of mechanisms, and evaluate the synchronicity of multiple chemical events.[55,56,62,67–69]

Five selected β-IBOs (ϕ1–ϕ5) show substantial displacement along the reaction coordinate from **RC*o*** to **PC*o*** via **TS*o*** (Figure 3-7). The corresponding α-IBOs are shown in Figures S3-6–S3-10. The first of these, ϕ1, corresponds to the π(O1–N1) bond of the nitrite moiety, which smoothly progresses to form the lone pair of the O1 atom. Similarly, ϕ2, ϕ3, ϕ4, and ϕ5 track the following transformations: lone pair(O1) → σ(O1–H1), σ(O3–H1) → lone pair(O3), π(Ar) → lone pair(N1), and σ(O1–N1) → lone pair(O1)′, respectively. These orbital transformations can be assigned to five elementary chemical events: the cleavage of the O1–N1 π-bond, the formation of the O1–H1 bond, the cleavage of the O3–H1 bond, the ET from Ar to nitrite, and the cleavage of the O1–N1 σ-bond. In

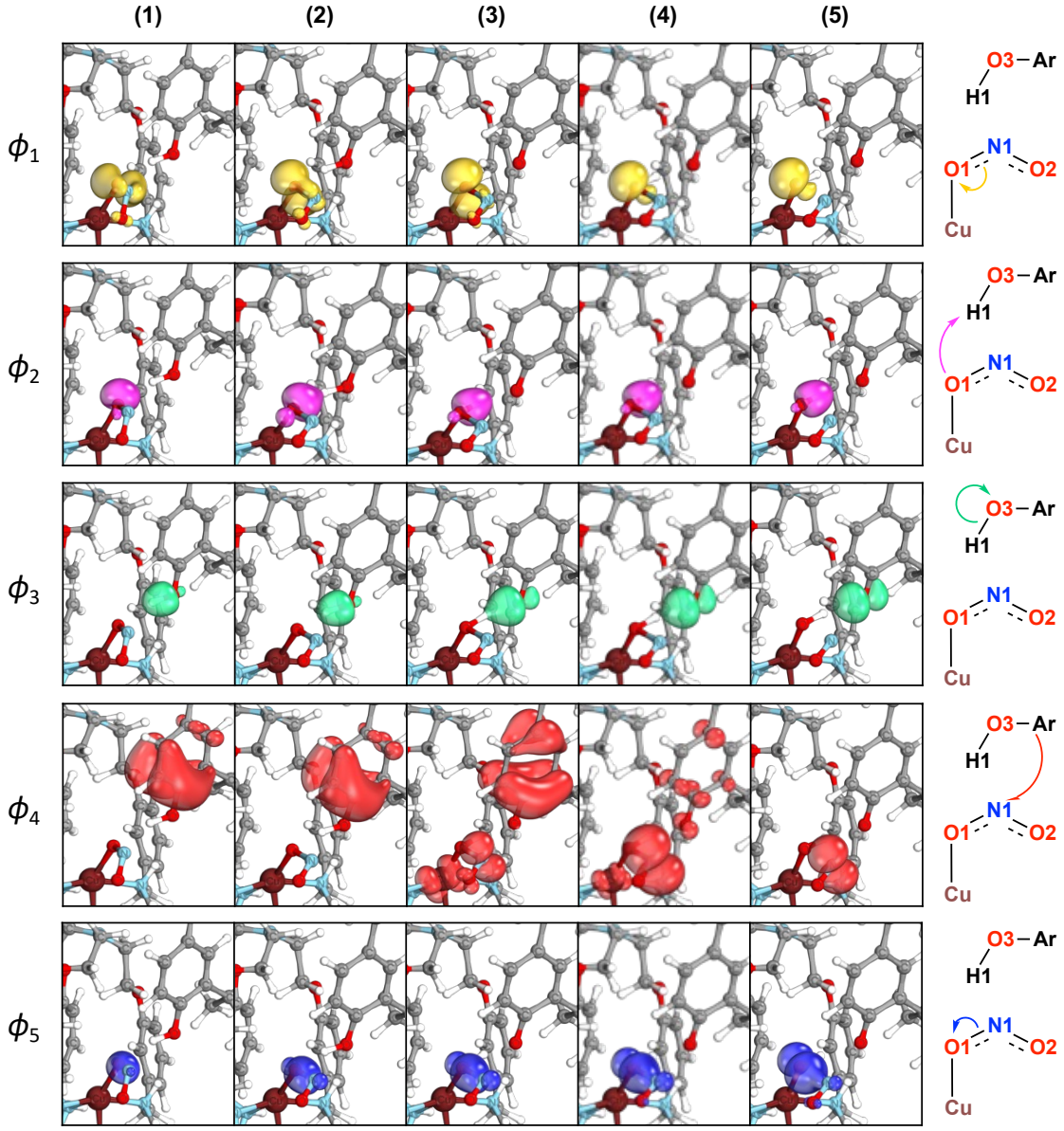

Figure 3-7. Transformation of selected β-IBOs (ϕ1–ϕ5) along intrinsic reaction coordinate for NO_2^- reduction from **RC*o*** to **PC*o*** via **TS*o***. The phase of IBOs is omitted for clarity. The curly arrows corresponding to the IBO changes are shown on the right.

ϕ1, ϕ2, ϕ3, and ϕ5, α- and β-IBOs behave similarly, indicating the flow of electron pairs. In particular, the fact that both the α- and β-IBOs for ϕ3 remain on the O3 atom means that the H1 atom is transferred as a proton. However, in ϕ4, the α- and β-IBOs behave differently. The α-IBO ϕ4 shows the migration of a π-cloud, π(Ar) → π(Ar)′, whereas the β-IBO ϕ4 represents π(Ar) → lone pair(N1), as previously described. Thus, the α- and β-IBOs for ϕ4 each indicate the flow of a single electron, not a pair.

To evaluate the concept of synchronicity of the five orbitals, we introduce "orbital change" as an indicator of the extent to which orbitals transform compared with their initial state. Orbital change is defined as the root-mean-square deviation of the orbital's partial charge distribution among the atoms from their initial charge distribution.[56,66,69] Figure 3-8 shows a plot of orbital changes for the five IBOs (ϕ1–ϕ5) along the reaction coordinate. The orbital change plots intuitively represent a progression of five elementary chemical events. Each of the five plots shows a substantial increase at different points, indicating asynchronous progress of the five elementary events. Their order is as follows: 1) O1–N1 π-bond cleavage; 2) O1–H1 bond formation; 3) O3–H1 bond cleavage; 4) ET from ArOH to nitrite; and 5) O1–N1 σ-bond cleavage. Among the five IBOs, the IBO ϕ1 corresponding to O1–N1 π-bond cleavage shows a sharp increase in orbital change at the

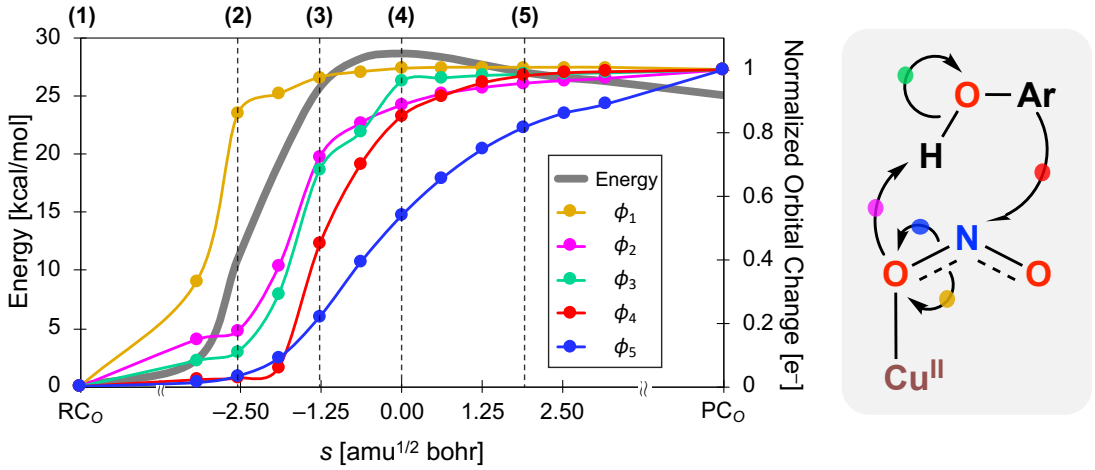

Figure 3-8. The IRC plots of relative energies and orbital changes of the five IBOs (ϕ1–ϕ5) shown in Figure 3-7. The numbers above the plots (in parentheses) correspond to the snapshot numbers in Figure 3-7. The transition state lies at s = 0.0 amu$^{1/2}$ bohr. The colors of the plotted lines correspond to the colors of the IBOs. The corresponding curly arrows are summarized on the right.

earliest point. This result is consistent with the IRC analysis results in Figure 3-6(a). The IBOs $\phi 2$ and $\phi 3$ show a substantial orbital change near the PT point (s = –1.72). Thus, the changes in $\phi 2$ and $\phi 3$ correspond to O–H bond formation and O–H bond cleavage, respectively. After that, the β-IBO $\phi 4$, which corresponds to the ET from ArOH to nitrite, changes as the reaction proceeds. The change in IBO $\phi 5$ progresses slowly after the changes of the IBOs $\phi 1 - \phi 4$ have occurred. Our orbital analysis provides useful information on the electronic structure changes associated with PT and ET, revealing that changes of the IBO are completely consistent with the IRC analysis. Also, the change in IBO $\phi 4$ indicates the transformation from an aromatic π-orbital into the lone pair of the N1 atom, indicating that this CPET mechanism contains PT and ET from the aromatic π-cloud. This is in good agreement with previous studies on the CPET mechanism related to phenol derivatives.[70–72] This result indicates that the reaction from **RC*o*** to **PC*o*** via **TS*o*** includes five elementary events, which proceed concertedly; furthermore, it indicates that they start with a timing gap for each other.

3.4. Conclusions

We used DFT calculations to investigate the mechanism for the reduction of NO_2^- to NO, mediated by a Cu(II) complex. On the basis of a geometry optimization, we obtained two types of $[CuNO_2]^+$ initial complexes: an O-coordinated Cu(II)–nitrite complex (**IC*O***) and an N-coordinated Cu(II)–nitro complex (**IC*N***). **IC*O*** and **IC*N*** differ in energy by 3.8 kcal/mol. The two initial complexes, **IC*O*** and **IC*N***, provide two reaction pathways: nitrite pathway and nitro pathway, respectively. The calculation results show that the nitrite pathway is achieved via one reaction step and proceeds via a transition state **TS*O*** in an endothermic way of 17.8 kcal/mol with an activation energy of 25.2 kcal/mol. The transition state corresponds to three chemical events: O–H bond cleavage, O–H bond formation, and O–N bond cleavage. By contrast, the nitro pathway is completed stepwise via two intermediates: $[Cu(I)HONO]^+$ and $[Cu(II)(NO)(OH)]^+$. The rate-determining step for the nitro pathway is the first step of the formation of $[Cu(I)HONO]^+$ via transition state **TS1*N*** with an activation energy of 22.8 kcal/mol. On the basis of these results, the nitrite pathway, **IC*O***-initiated concerted pathway, and the nitro pathway, **IC*N***-initiated stepwise pathway, are comparable. DFT calculations suggest that the tripodal-heteroditopic-cryptand ligand plays no significant role in the nitrite reduction by the copper(II) complex. Thus, this reaction mechanism can be extended to the nitrite reduction using a copper complex which has the similar ligand field and phenol derivative as a reductant. We also performed an IRC analysis to precisely characterize each reaction step. The results showed that the two reaction pathways are achieved by CPET. In the nitrite pathway, CPET coupled with O–N bond cleavage occurs to form product complex $[Cu(II)OH]^+$, NO, and $ArO^{\bullet}$. In the first step of the nitro pathway, CPET occurs to form $[Cu(I)HONO]^+$ and $ArO^{\bullet}$. Moreover, the IRC analysis determined the location of PT and ET as a unit of the s value. Therefore, by using Δs, the difference between the PT and ET points, as an index, the (a)synchronicity of PT and ET in the CPET reaction can now be evaluated. In the nitrite pathway, PT point between **RC*O*** and **PC*O*** is earlier than ET point by $\Delta s = 1.65$, in which the reaction is a *basic asynchronous* CPET. In contrast, in the nitro pathway, PT and ET points between **RC*N*** and **IM1*N*** are close ($\Delta s = 0.11$), in which the reaction is *synchronous* CPET. Although the two pathways lead to the same products—

[Cu(II)OH]$^{+}$, NO, and ArO$^{\bullet}$—their CPET mechanisms differ substantially with respect to the asynchronicity of PT and ET. Thus, by tracking the continuous change in electronic structure *via* IRC analysis, we successfully described the CPET behavior in the NO_2^- reduction. The concept of PT and ET points will facilitate the characterization and understanding of CPET reactions.

References

1. Richardson, D. J.; Watmough, N. J. Inorganic Nitrogen Metabolism in Bacteria. *Curr. Opin. Chem. Biol.* **1999**, *3*, 207-219.
2. Canfield, D. E.; Glazer, A. N.; Falkowski, P. G. The Evolution and Future of Earth's Nitrogen Cycle. *Science* **2010**, *330*, 192-196.
3. Timmons, A. J.; Symes, M. D. Converting between the Oxides of Nitrogen Using Metal-Ligand Coordination Complexes. *Chem. Soc. Rev.* **2015**, *44*, 6708-6722.
4. Averill, B. A. Dissimilatory Nitrite and Nitric Oxide Reductases. *Chem. Rev.* **1996**, *96*, 2951-2964.
5. Lehnert, N.; Kim, E.; Dong, H. T.; Harland, J. B.; Hunt, A. P.; Manickas, E. C.; Oakley, K. M.; Pham, J.; Reed, G. C.; Alfaro, V. S. The biologically relevant coordination chemistry of iron and nitric oxide: electronic structure and reactivity. *Chem. Rev.* **2021**, *121*, 14682-14905.
6. Maia, L. B.; Moura, J. J. G. How Biology Handles Nitrite. *Chem. Rev.* **2014**, *114*, 5273-5357.
7. Besson, S.; Almeida, M. G.; Silveira, C. M. Nitrite Reduction in Bacteria: A Comprehensive View of Nitrite Reductases. *Coord. Chem. Rev.* **2022**, *464*, 214560.
8. Dodd, F. E.; Van Beeumen, J.; Eady, R. R.; Hasnain, S. S. X-Ray Structure of a Blue-Copper Nitrite Reductase in Two Crystal Forms. The Nature of the Copper Sites, Mode of Substrate Binding and Recognition by Redox Partner. *J. Mol. Biol.* **1998**, *282*, 369-382.
9. MacPherson, I. S.; Murphy, M. E. P. Type-2 Copper-Containing Enzymes. *Cell. Mol. Life Sci.* **2007**, *64*, 2887-2899.
10. Fülöp, V.; Moir, J. W. B.; Ferguson, S. J.; Hajdu, J. The Anatomy of a Bifunctional Enzyme: Structural Basis for Reduction of Oxygen to Water and Synthesis of Nitric Oxide by Cytochrome Cd1. *Cell* **1995**, *81*, 369-377.
11. Williams, P. A.; Fülöp, V.; Garman, E. F.; Saunders, N. F. W.; Ferguson, S. J.; Hajdu, J. Haem-Ligand Switching during Catalysis in Crystals of a Nitrogen-Cycle Enzyme. *Nature* **1997**, *389*, 406-412.
12. Culotta, E.; Koshland, D. E. NO News Is Good News. *Science* **1992**, *258*, 1862-1865.

13. Lundberg, J. O.; Weitzberg, E.; Gladwin, M. T. The Nitrate-Nitrite-Nitric Oxide Pathway in Physiology and Therapeutics. *Nat. Rev. Drug Discov*. **2008**, *7*, 156-167.
14. Lundberg, J. O.; Gladwin, M. T.; Weitzberg, E. Strategies to Increase Nitric Oxide Signalling in Cardiovascular Disease. *Nat. Rev. Drug Discov.* **2015**, *14*, 623-641.
15. Wang, J.; Keceli, G.; Cao, R.; Su, J.; Mi, Z. Molybdenum-Containing Nitrite Reductases: Spectroscopic Characterization and Redox Mechanism. *Redox Rep.* **2017**, *22*, 17-25.
16. Bender, D.; Schwarz, G. Nitrite-Dependent Nitric Oxide Synthesis by Molybdenum Enzymes. *FEBS Lett.* **2018**, *592*, 2126-2139.
17. Sparacino-Watkins, C. E.; Tejero, J.; Sun, B.; Gauthier, M. C.; Thomas, J.; Ragireddy, V.; Merchan, B. A.; Wang, J.; Azarov, I.; Basu, P.; Gladwin, M. Nitrite reductase and nitric-oxide synthase activity of the mitochondrial molybdopterin enzymes mARC1 and mARC2. *J. Biol. Chem.* **2014**, *289*, 10345-10358.
18. Gladwin, M. T.; Grubina, R.; Doyle, M. P. The new chemical biology of nitrite reactions with hemoglobin: R-state catalysis, oxidative denitrosylation, and nitrite reductase/anhydrase. *Acc. Chem. Res.* **2009**, *42*, 157-167.
19. Komeda, N.; Nagao, H.; Kushi, Y.; Adachi, G.; Suzuki, M.; Uehara, A.; Tanaka, K. Molecular Structure of Nitro- and Nitrito-Copper Complexes as Reaction Intermediates in Electrochemical Reduction of Nitrite to Dinitrogen Oxide. *Bull. Chem. Soc. Jpn.* **1995**, *68*, 581-589.
20. Woollard-Shore, J. G.; Holland, J. P.; Jones, M. W.; Dilworth, J. R. Nitrite Reduction by Copper Complexes. *Dalton Trans.* **2010**, *39*, 1576-1585.
21. Chang, Y. L.; Chen, H. Y.; Chen, S. H.; Kao, C. L.; Chiang, M. Y.; Hsu, S. C. N. An Investigation on Catalytic Nitrite Reduction Reaction by Bioinspired CuII Complexes. *Dalton Trans.* **2022**, *51*, 7715-7722.
22. Burg, A.; Lozinsky, E.; Cohen, H.; Meyerstein, D. Mechanism of Reduction of the Nitrite Ion by CuI Complexes. *Eur. J. Inorg. Chem.* **2004**, *18*, 3675-3680.
23. Chuang, W. J.; Lin, I. J.; Chen, H. Y.; Chang, Y. L.; Hsu, S. C. N. Characterization of a New Copper(I)-Nitrito Complex That Evolves Nitric Oxide. *Inorg. Chem.* **2010**, *49*, 5377-5384.
24. Hsu, S. C. N.; Chang, Y. L.; Chuang, W. J.; Chen, H. Y.; Lin, I. J.; Chiang, M. Y.;

Kao, C. L.; Chen, H. Y. Copper(I) Nitro Complex with an Anionic [HB(3,5-Me2Pz) 3]- Ligand: A Synthetic Model for the Copper Nitrite Reductase Active Site. *Inorg. Chem.* **2012**, *51*, 9297-9308.

25. Kumar, M.; Dixon, N. A.; Merkle, A. C.; Zeller, M.; Lehnert, N.; Papish, E. T. Hydrotris(Triazolyl)Borate Complexes as Functional Models for Cu Nitrite Reductase: The Electronic Influence of Distal Nitrogens. *Inorg. Chem.* **2012**, *51*, 7004-7006.
26. Hunt, A. P.; Batka, A. E.; Hosseinzadeh, M.; Gregory, J. D.; Haque, H. K.; Ren, H.; Meyerhoff, M. E.; Lehnert, N. Nitric oxide generation on demand for biomedical applications via electrocatalytic nitrite reduction by copper BMPA-and BEPA-carboxylate complexes. *ACS Catal.* **2019**, *9*, 7746-7758.
27. Maji, R. C.; Barman, S. K.; Roy, S.; Chatterjee, S. K.; Bowles, F. L.; Olmstead, M. M.; Patra, A. K. Copper Complexes Relevant to the Catalytic Cycle of Copper Nitrite Reductase: Electrochemical Detection of NO(g) Evolution and Flipping of NO 2 Binding Mode upon CuII → CuI Reduction. *Inorg. Chem.* **2013**, *52*, 11084-11095.
28. Sakhaei, Z.; Kundu, S.; Donnelly, J. M.; Bertke, J. A.; Kim, W. Y.; Warren, T. H. Nitric Oxide Release via Oxygen Atom Transfer from Nitrite at Copper(II). *Chem. Commun.* **2017**, *53*, 549-552.
29. Kundu, S.; Kim, W. Y.; Bertke, J. A.; Warren, T. H. Copper(II) Activation of Nitrite: Nitrosation of Nucleophiles and Generation of NO by Thiols. *J. Am. Chem. Soc.* **2017**, *139*, 1045-1048.
30. Maji, R. C.; Mishra, S.; Bhandari, A.; Singh, R.; Olmstead, M. M.; Patra, A. K. A Copper(II) Nitrite That Exhibits Change of Nitrite Binding Mode and Formation of Copper(II) Nitrosyl Prior to Nitric Oxide Evolution. *Inorg. Chem.* **2018**, *57*, 1550-1561.
31. Chang, Y. L.; Lin, Y. F.; Chuang, W. J.; Kao, C. L.; Narwane, M.; Chen, H. Y.; Chiang, M. Y.; Hsu, S. C. N. Structure and Nitrite Reduction Reactivity Study of Bio-Inspired Copper(i)-Nitro Complexes in Steric and Electronic Considerations of Tridentate Nitrogen Ligands. *Dalton Trans.* **2018**, *47*, 5335-5341.
32. Maria, S.; Chattopadhyay, T.; Ananya, S.; Kundu, S. Reduction of Nitrite to NO at

a Mononuclear Copper(II)-Phenolate Site. *Inorganica Chim. Acta* **2020**, *506*, 119515.

33. Ghosh, S.; Dey, A.; Sun, Y.; Scholes, C. P.; Solomon, E. I. Spectroscopic and Computational Studies of Nitrite Reductase: Proton Induced Electron Transfer and Backbonding Contributions to Reactivity. *J. Am. Chem. Soc.* **2009**, *131*, 277-288.
34. Li, Y.; Hodak, M.; Bernholc, J. Enzymatic Mechanism of Copper-Containing Nitrite Reductase. *Biochemistry* **2015**, *54*, 1233-1242.
35. Cioncoloni, G.; Roger, I.; Wheatley, P. S.; Wilson, C.; Morris, R. E.; Sproules, S.; Symes, M. D. Proton-Coupled Electron Transfer Enhances the Electrocatalytic Reduction of Nitrite to NO in a Bioinspired Copper Complex. *ACS Catal.* **2018**, *8*, 5070-5084.
36. Moore, C. M.; Szymczak, N. K. Nitrite Reduction by Copper through Ligand-Mediated Proton and Electron Transfer. *Chem. Sci.* **2015**, *6*, 3373-3377.
37. Mondal, A.; Reddy, K. P.; Bertke, J. A.; Kundu, S. Phenol Reduces Nitrite to NO at Copper(II): Role of a Proton-Responsive Outer Coordination Sphere in Phenol Oxidation. *J. Am. Chem. Soc.* **2020**, *142*, 1726-1730.
38. Becke, A. D. Density-functional exchange-energy approximation with correct asymptotic behavior. *Phys. Rev. A* **1988**, *38*, 3098-3100.
39. Lee, C.; Yang, W.; Parr, R. G. Development of the Colle-Salvetti correlation-energy formula into a functional of the electron density. *Phys. Rev. B: Condens. Matter Mater. Phys.* **1988**, *37*, 785-789.
40. Becke, A. D. Density-functional thermochemistry. III. The role of exact exchange. *J. Chem. Phys.* **1993**, *98*, 5648-5652.
41. Gaussian 16, Revision A.03, Frisch, M. J.; Trucks, G. W.; Schlegel, H. B.; Scuseria, G. E.; Robb, M. A.; Cheeseman, J. R.; Scalmani, G.; Barone, V.; Petersson, G. A.; Nakatsuji, H.; Li, X.; Caricato, M.; Marenich, A. V.; Bloino, J.; Janesko, B. G.; Gomperts, R.; Mennucci, B.; Hratchian, H. P.; Ortiz, J. V.; Izmaylov, A. F.; Sonnenberg, J. L.; Williams-Young, D.; Ding, F.; Lipparini, F.; Egidi, F.; Goings, J.; Peng, B.; Petrone, A.; Henderson, T.; Ranasinghe, D.; Zakrzewski, V. G.; Gao, J.; Rega, N.; Zheng, G.; Liang, W.; Hada, M.; Ehara, M.; Toyota, K.; Fukuda, R.; Hasegawa, J.; Ishida, M.; Nakajima, T.; Honda, Y.; Kitao, O.; Nakai, H.; Vreven,

T.; Throssell, K.; Montgomery, J. A., Jr.; Peralta, J. E.; Ogliaro, F.; Bearpark, M. J.; Heyd, J. J.; Brothers, E. N.; Kudin, K. N.; Staroverov, V. N.; Keith, T. A.; Kobayashi, R.; Normand, J.; Raghavachari, K.; Rendell, A. P.; Burant, J. C.; Iyengar, S. S.; Tomasi, J.; Cossi, M.; Millam, J. M.; Klene, M.; Adamo, C.; Cammi, R.; Ochterski, J. W.; Martin, R. L.; Morokuma, K.; Farkas, O.; Foresman, J. B.; Fox, D. J. Gaussian, Inc., Wallingford CT, 2016.

42. Wachters, A. J. H. Gaussian basis set for molecular wavefunctions containing third-row atoms. *J. Chem. Phys.* **1970**, *52*, 1033-1036.
43. Hay, P. J. Gaussian basis sets for molecular calculations – representation of 3D orbitals in transition-metal atoms. *J. Chem. Phys.* **1977**, *66* 4377-4384.
44. Raghavachari, K.; Trucks, G. W. Highly correlated systems: Excitation energies of first row transition metals Sc-Cu. *J. Chem. Phys.* **1989**, *91*, 1062-1065.
45. Hehre, W. J.; Ditchfield, R.; Pople, J. A. Self-Consistent Molecular Orbital Methods. 12. Further extensions of Gaussian-type basis sets for use in molecular-orbital studies of organic-molecules. *J. Chem. Phys.* **1972**, *56*, 2257-2261.
46. Hariharan, P. C.; Pople, J. A. The influence of polarization functions on molecular-orbital hydrogenation energies. *Theoret. Chim. Acta* **1973**, *28* 213-222.
47. Petersson, G. A.; Al-Laham, M. A. A complete basis set model chemistry. II. Open-shell systems and the total energies of the first-row atoms. *J. Chem. Phys.* **1991**, *94*, 6081-6090.
48. Schwabe, T.; Grimme, S. Double-hybrid density functionals with long-range dispersion corrections: higher accuracy and extended applicability. *Phys. Chem. Chem. Phys.* **2007**, *9*, 3397-3406.
49. Grimme, S.; Antony, J.; Ehrlich, S.; Krieg, H. A consistent and accurate ab initio parametrization of density functional dispersion correction (DFT-D) for the 94 elements H-Pu. *J. Chem. Phys.* **2010**, *132*, 154104-154119.
50. Liakos, D. G.; Neese, F. Interplay of correlation and relativistic effects in correlated calculations on transition-metal complexes: The $(Cu_2O_2)^{2+}$ core revisited. *J. Chem. Theory Comput.* **2011**, *7*, 1511-1523.
51. Tomasi, J.; Mennucci, B.; Cammi, R. Quantum mechanical continuum solvation models. *Chem. Rev.* **2005**, *105*, 2999-3094.

52. Fukui, K. Formulation of the reaction coordinate. *J. Phys. Chem.* **1970**, *74*, 4161-4163.

53. Fukui, K. The path of chemical reactions-the IRC approach. *Acc. Chem. Res.* **1981**, *14*, 363-368.

54. Knizia, G. Intrinsic Atomic Orbitals: An Unbiased Bridge between Quantum Theory and Chemical Concepts. *J. Chem. Theory Comput.* **2013**, *9*, 4834-4843.

55. Knizia, G.; Klein, J. E. M. N. Electron Flow in Reaction Mechanisms-Revealed from First Principles. *Angew. Chem., Int. Ed.* **2015**, *54*, 5518-5522.

56. Klein, J. E. M. N.; Knizia, G. CPCET versus HAT: A Direct Theoretical Method for Distinguishing X-H Bond-Activation Mechanisms. *Angew. Chem., Int. Ed.* **2018**, *57*, 11913-11917.

57. Weigend, F.; Ahlrichs, R. Balanced basis sets of split valence, triple zeta valence and quadruple zeta valence quality for H to Rn: Design and assessment of accuracy. *Phys. Chem. Chem. Phys.* **2005**, *7*, 3297-3305.

58. Weigend, F. Accurate Coulomb-fitting basis sets for H to Rn. *Phys. Chem. Chem. Phys.* **2006**, *8*, 1057-1065.

59. Ahlrichs, R.; Bär, M.; Häser, M.; Horn, H.; Kölmel, C. Electronic structure calculations on workstation computers: The program system turbomole. *Chem. Phys. Lett.* **1989**, *162*, 165-169.

60. Bím, D.; Maldonado-Domínguez, M.; Rulíšek, L.; Srnec, M. Beyond the classical thermodynamic contributions to hydrogen atom abstraction reactivity. *Proc. Natl. Acad. Sci. U.S.A.* **2018**, *115*, E10287-E10294.

61. Darcy, J. W.; Kolmar, S. S.; Mayer, J. M. Transition State Asymmetry in C–H Bond Cleavage by Proton-Coupled Electron Transfer. *J. Am. Chem. Soc.* **2019**, *141*, 10777-10787.

62. Goetz, M. K.; Anderson, J. S. Experimental Evidence for pK_a-Driven Asynchronicity in C-H Activation by a Terminal Co(III)-Oxo Complex. *J. Am. Chem. Soc.* **2019**, *141*, 4051-4062.

63. Kotani, H.; Shimomura, H.; Ikeda, K.; Ishizuka, T.; Shiota, Y.; Yoshizawa, K.; Kojima, T. Mechanistic Insight into Concerted Proton-Electron Transfer of a Ru(IV)-Oxo Complex: A Possible Oxidative Asynchronicity. *J. Am. Chem. Soc.*

2020, *142*, 16982-16989.

64. Coste, S. C.; Brezny, A. C.; Koronkiewicz, B.; Mayer, J. M. C–H oxidation in fluorenyl benzoates does not proceed through a stepwise pathway: revisiting asynchronous proton-coupled electron transfer. *Chem. Sci.*, **2021**, *12*, 13127-13136.
65. Tyburski, R.; Liu, T. F.; Glover, S. D.; Hammarström, L. Proton-Coupled Electron Transfer Guidelines, Fair and Square. *J. Am. Chem. Soc.*, **2021**, *143*, 560-576.
66. Zhang, J.; Lee, Y. M.; Seo, M. S.; Kim, Y.; Lee, E.; Fukuzumi, S.; Nam, W. Oxidative versus basic asynchronous hydrogen atom transfer reactions of Mn(iii)-hydroxo and Mn(iii)-aqua complexes. *Inorg. Chem. Front.* **2022**, *9*, 3233-3243.
67. Mandal, M.; Elwell, C. E.; Bouchey, C. J.; Zerk, T. J.; Tolman, W. B.; Cramer, C. J. Mechanisms for Hydrogen-Atom Abstraction by Mononuclear Copper(III) Cores: Hydrogen-Atom Transfer or Concerted Proton-Coupled Electron Transfer? *J. Am. Chem. Soc.* **2019**, *141*, 17236-17244.
68. Curtolo, F.; Arantes, G. M. Mechanisms for Flavin-Mediated Oxidation: Hydride or Hydrogen-Atom Transfer? *J. Chem. Inf. Model.* **2020**, *60*, 6282-6287.
69. Ikeda, K.; Mahyuddin, M. H.; Shiota, Y.; Yoshizawa, K. Active Catalyst for Methane Hydroxylation by an Iridium-Oxo Complex. *ACS Catal.* **2020**, *10*, 8254-8262.
70. DiLabio, G. A.; Johnson, E. R. Lone pair−π and π−π interactions play an important role in proton-coupled electron transfer reactions. *J. Am. Chem. Soc.* **2007**, *129*, 6199-6203.
71. Karas, L. J.; Wu, C.-H.; Wu, J. I. Barrier-Lowering Effects of Baird Antiaromaticity in Photoinduced Proton-Coupled Electron Transfer (PCET) Reactions. *J. Am. Chem. Soc.* **2021**, *143*, 17970-17974.
72. Mena, L. D.; Baumgartner, M. T. Chalcogen Atoms as Electron Donors in Proton-Coupled Electron Transfer Reactions. *J. Am. Chem. Soc.* **2022**, *144*, 15922-15927.

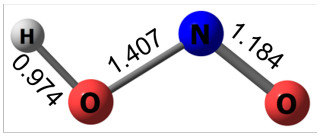

Figure S3-1. Optimized structure of nitrous acid molecule. Bond distance is given in unit of Å.

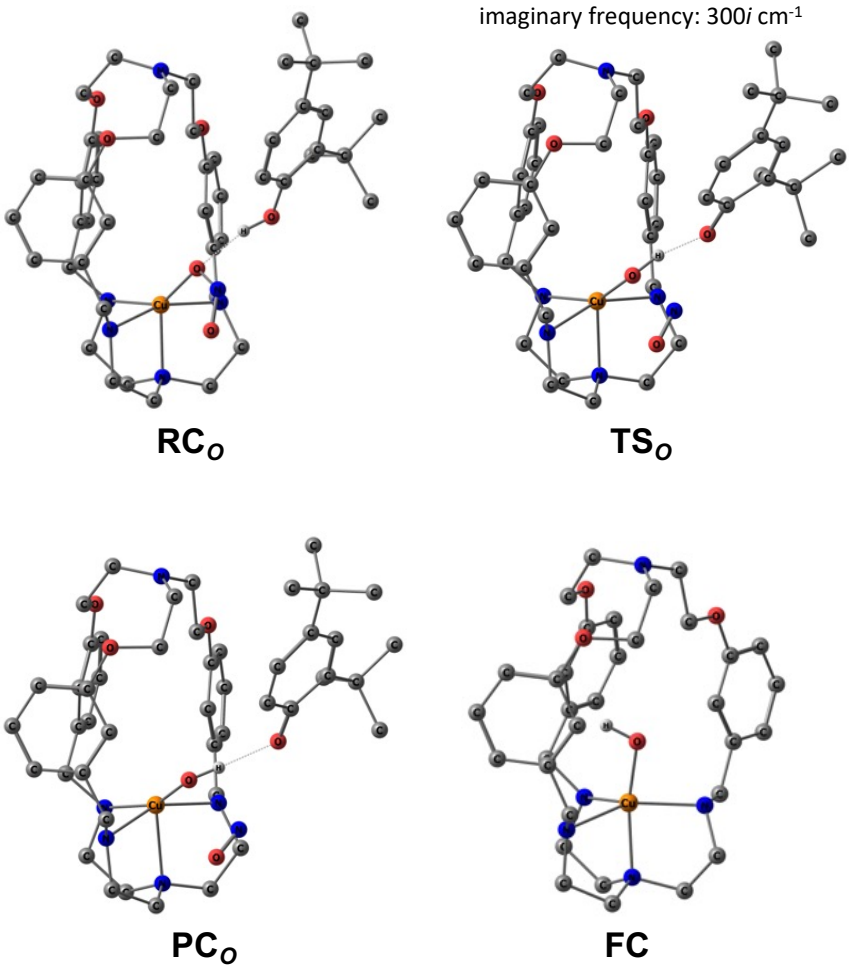

Figure S3-2. Overall structures of all species in the nitrite pathway. H atoms are omitted for clarity.

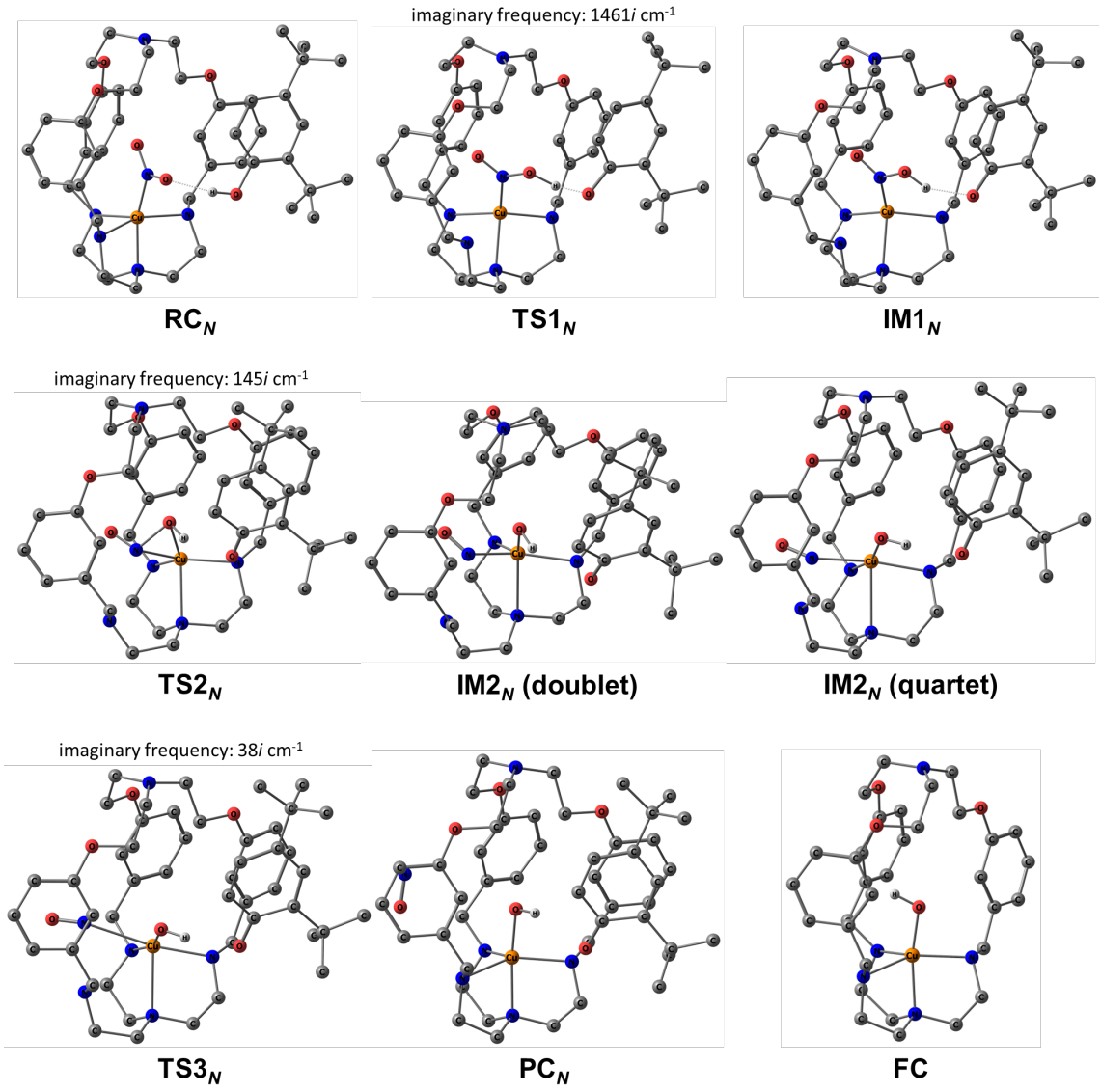

Figure S3-3. Overall structures of all species in the nitro pathway. H atoms are omitted for clarity.

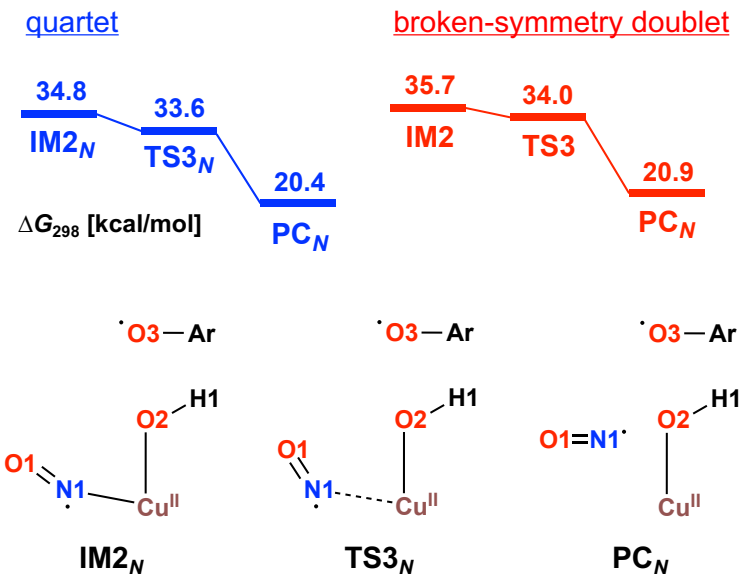

Figure S3-4. The free energy diagram for the reaction step **IM2$_N$→TS3$_N$→PC$_N$** in the quartet and broken-symmetry doublet states.

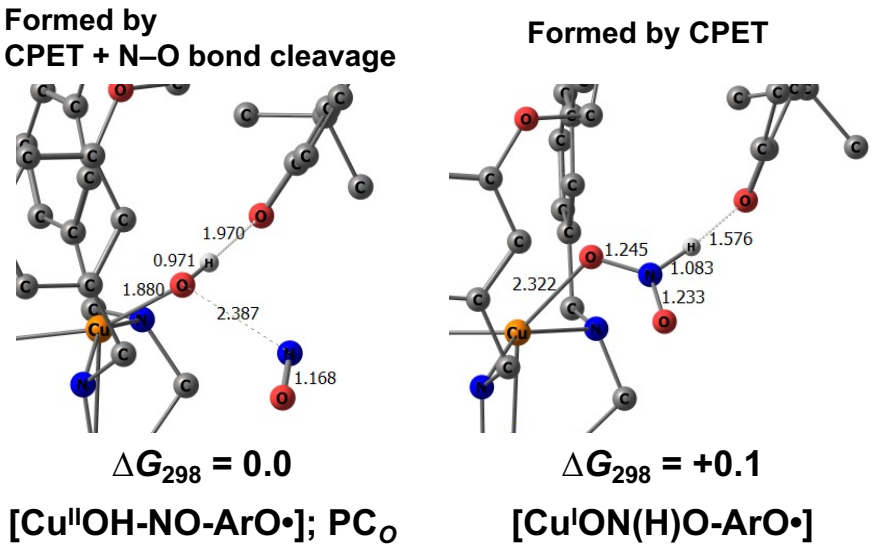

Figure S3-5. Optimized structures of **PC$_O$** and a byproduct formed by H-atom migration from ArO to the N1 atom.

O1–N1 σ-bond

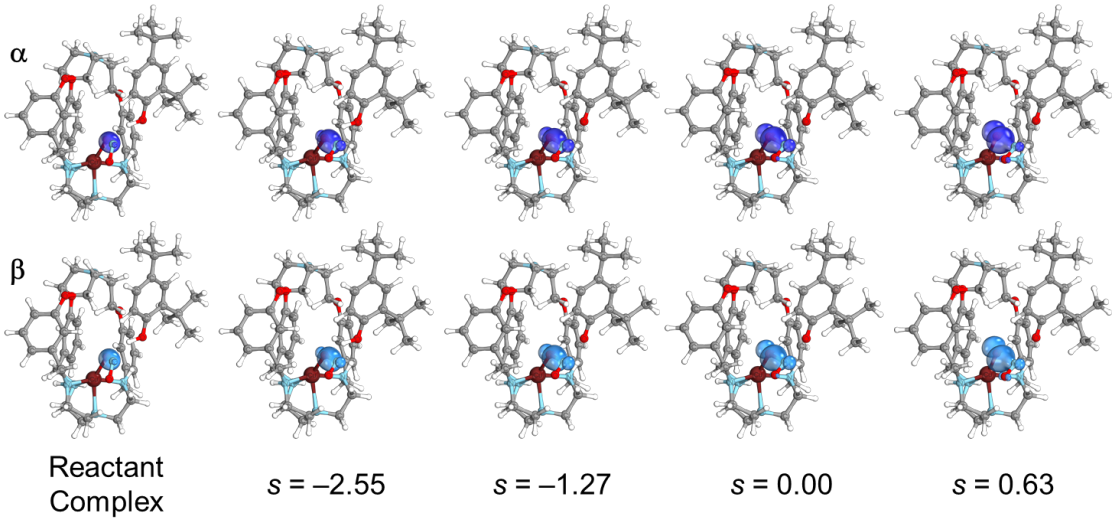

Figure S3-6. Transformation of O–N σ-bond IBO.

O1–N1 π-bond

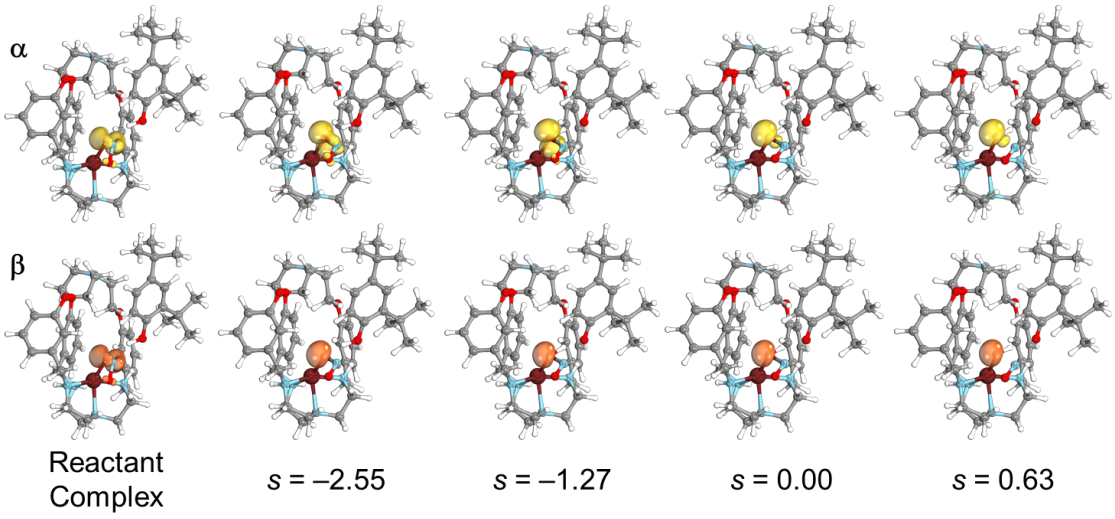

Figure S3-7. Transformation of O–N π-bond IBO.

π-system of ArOH

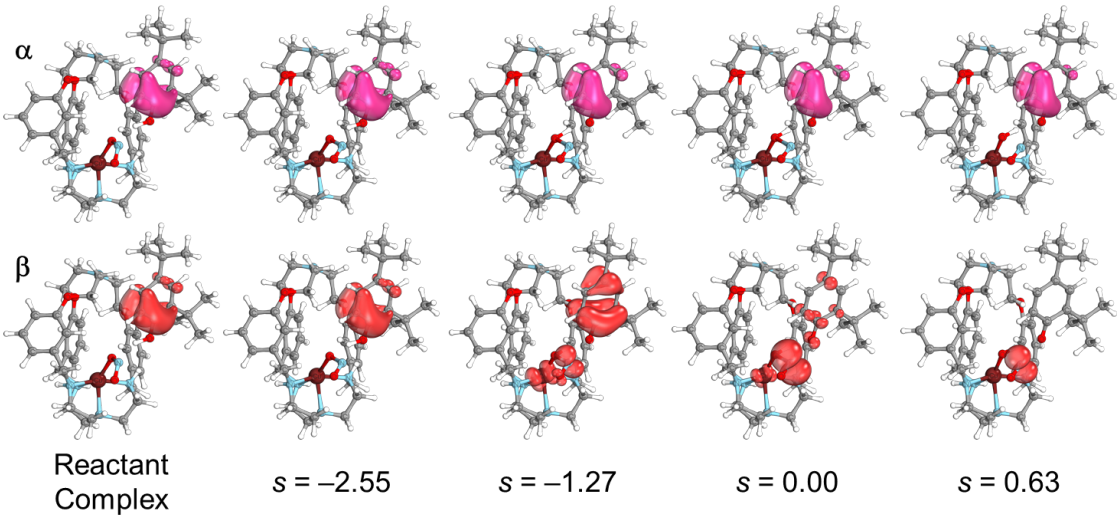

Figure S3-8. Transformation of IBO for π-system of ArOH.

O3–H1 σ-bond

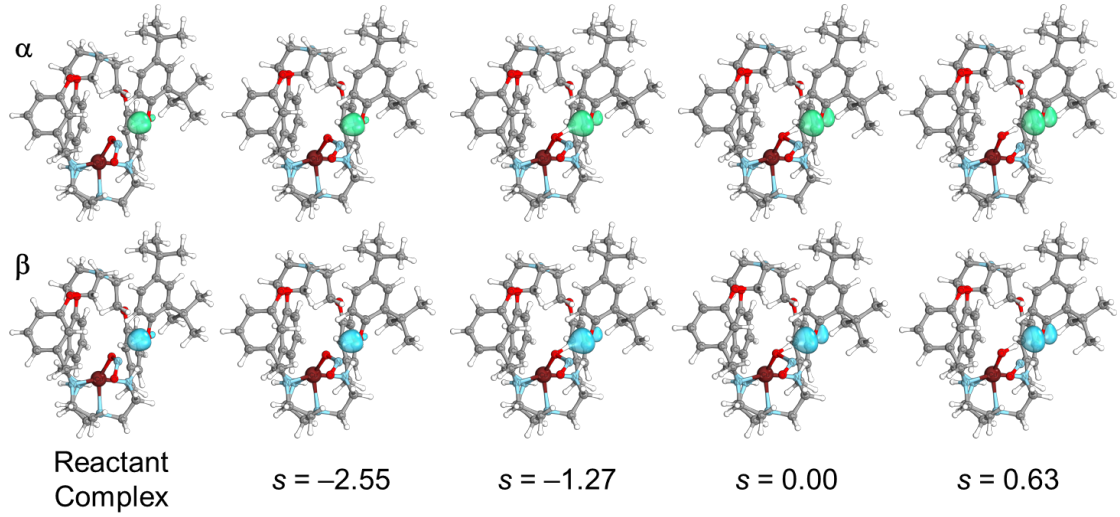

Figure S3-9. Transformation of O–H σ-bond IBO.

Lone pair of O3 atom

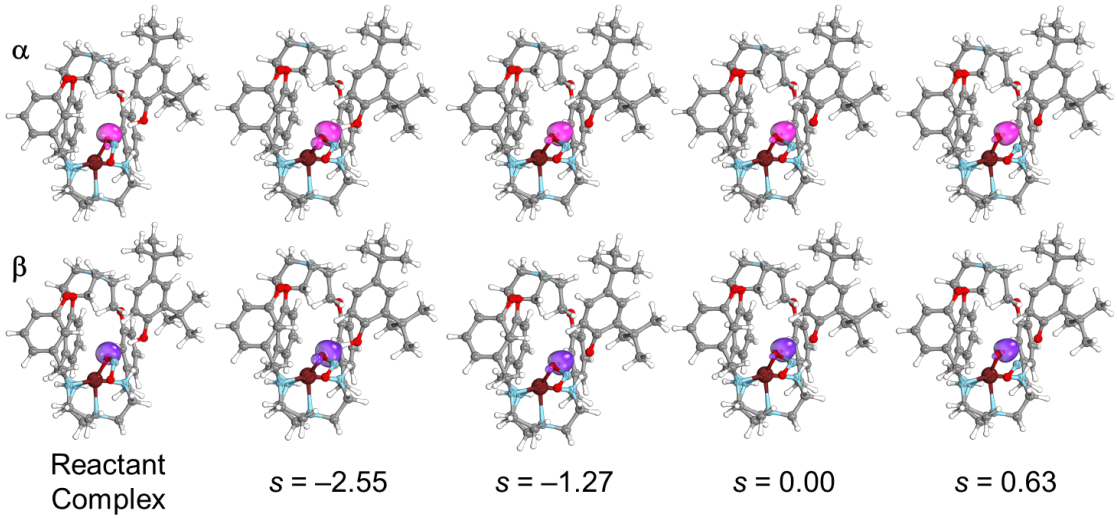

Figure S3-10. Transformation of IBO for lone pair of O atom.

Chapter 4. General Conclusions

This dissertation exhibited the mechanistic aspects of two important NO_x reduction reactions mediated by transition metal complexes; reduction of NO to N_2O by a dicopper complex and reduction of NO_2^- to NO by a monocopper complex.

In Chapter 2, the mechanism of the reduction of NO to N_2O mediated by a dicopper complex is discussed. The computational results indicated that the reaction consists of three fundamental steps: (1) N–N bond formation, (2) isomerization of the N_2O_2 moiety, and (3) N–O bond cleavage. The calculated reaction mechanism predicts the initial coupling of two NO molecules. These results are consistent with experimental observations, where N_2O is released in the presence of the dicopper complex. Additionally, the large binding energy of NO and Cu atoms in the reactant complex $[Cu_2(NO)_2]^{2+}$ and the small binding energy of N_2O in the product complex $[Cu_2(N_2O)(\mu\text{-}O)]^{2+}$ favor this catalytic cycle. Thus, DFT calculations enable us to understand the frequent electron transfer (ET) between Cu and the ligand in addition to structural changes in the reaction mechanism, providing a useful tool for analyzing reaction pathways and revealing the details of the sequential N–N bond formation, isomerization of N_2O_2, and N–O bond cleavage reactions.

In Chapter 3, the author investigated the mechanism of the reduction of NO_2^- to NO by a Cu(II) complex using DFT calculations. According to geometry optimization, we identified two types of $[CuNO_2]^+$ initial complexes, i.e., an O-coordinated Cu(II)–nitrite complex (**IC*O***) and an N-coordinated Cu(II)–nitro complex (**IC*N***), which allowed proposing the nitrite and nitro reaction pathways, respectively. Given their energy profiles, the two pathways are comparable. In addition, to determine the exact nature of the concerted proton-electron transfer (CPET) reactions in both pathways, changes in the geometric and electronic structures were analyzed using an intrinsic reaction coordinate (IRC) analysis. The points of proton transfer (PT) and electron transfer (ET) were introduced to evaluate the asynchronicity of PT and ET in a CPET reaction using the difference between the PT and ET points ($\Delta s = s(\mathrm{PT}) - s(\mathrm{ET})$, where the s value represents the location of PT and ET). In the nitrite pathway, $\Delta s = -1.65$, indicating that the PT point precedes the ET point, that is the reaction is a basic asynchronous CPET. In contrast, in

the nitro pathway, the reaction is a synchronous CPET because the PT and ET points are close (Δs = −0.11). Although the two pathways lead to the same products, i.e., $[Cu(II)OH]^+$, NO, and $ArO^{\bullet}$, their CPET mechanisms differ substantially in terms of the asynchronicity of PT and ET. Thus, by tracking the continuous change in electronic structure via IRC analysis, we successfully described the CPET behavior in the NO_2^- reduction. The concept of PT and ET points facilitates the characterization and understanding of CPET reactions.

A reaction mechanism is a theoretical deduction that provides a comprehensive description of how molecules transform into products during a chemical reaction. Only a restricted subset of the reaction mechanism can be observed experimentally. For example, initially, only stable products or intermediates could be isolated, while unstable intermediates and transition states were unobservable. However, the advent of crystallography and spectroscopy has enabled the observation of metastable chemical species that emerge during a reaction. Concurrently, advancements in reaction kinetics, including transition state theory, have significantly contributed to the elucidation of reaction mechanisms. Consequently, a reliable reaction mechanism can be proposed by integrating diverse experimental techniques and synthesizing their findings.

Currently, DFT calculations are employed by numerous researchers as a highly effective tool for analyzing reaction mechanisms. Initially, it was challenging to optimize the structure of even a simple organic molecule comprising a few dozen atoms. However, due to advancements in computer performance, it is now possible to handle molecules comprising over 100 atoms and transition metal elements at a practical level. Consequently, the role of DFT calculations is evolving, moving from “calculations that reproduce experiments” to “calculations that drive experiments.”

In this dissertation, the author has elucidated key mechanistic pathways and electronic structures involved in the NO_x reduction reactions catalyzed by copper complexes, using DFT calculations. These findings highlight not only the utility of DFT calculations to unravel complicated reaction mechanisms but also their potential to provide novel perspectives that are challenging to observe experimentally. These contributions lay a robust foundation for the rational design of next-generation transition metal catalysts aimed at enhancing the efficiency and selectivity of NO_x reduction reactions.

List of Publications

1. Chen, L.; **Kametani, Y.**; Imamura, K.; Abe, T.; Shiota, Y.; Yoshizawa, K.; Hisaeda, Y.; Shimakoshi, H. Visible Light-Driven Cross-Coupling Reactions of Alkyl Halides with Phenylacetylene Derivatives for C(sp^3)-C(sp) Bond Formation Catalyzed by a B_{12} Complex. *Chem. Commun.* **2019**, *55* (87), 13070-13073. DOI: 10.1039/C9CC06185A.
2. Abe, T.; **Kametani, Y.**; Yoshizawa, K.; Shiota, Y. Mechanistic Insights into the Dicopper-Complex-Catalyzed Hydroxylation of Methane and Benzene Using Nitric Oxide: A DFT Study. *Inorg. Chem.* **2021**, *60* (7), 4599-4609. DOI: 10.1021/acs.inorgchem.0c03558.
3. **Kametani, Y.**; Abe, T.; Yoshizawa, K.; Shiota, Y. Mechanistic Study on Reduction of Nitric Oxide to Nitrous Oxide Using a Dicopper Complex. *Dalton Trans.* **2022**, *51* (14), 5399-5403. DOI: 10.1039/D2DT00132H.
4. Kamada, K.; Jung, J.; **Kametani, Y.**; Wakabayashi, T.; Shiota, Y.; Yoshizawa, K.; Bae, S. H.; Muraki, M.; Naruto, M.; Sekizawa, K.; Sato, S.; Morikawa, T.; Saito, S. Importance of Steric Bulkiness of Iridium Photocatalysts with PNNP Tetradentate Ligands for CO_2 Reduction. *Chem. Commun.* **2022**, *58* (66), 9218-9221. DOI: 10.1039/D2CC03689B.
5. Chen, T. W. M.; Tanaka, Y.; **Kametani, Y.**.; Cheng, K. Y.; Lin, C. H.; Lin, Y. R.; Hsu, T. R.; Chen, Z. Q.; Hao, J. P.; Mori, S.; Shiota, Y.; Yoshizawa, K.; Furuta, H.; Shimizu, S.; Chen, C. H. Spontaneous Assembly and Three-Dimensional Stacking of Antiaromatic 5,15-Dioxaporphyrin on HOPG. *Angew. Chem., Int. Ed.* **2022**, *61* (48), e202212726. DOI: 10.1002/anie.202212726.
6. Shichijo, K.; **Kametani, Y.**.; Shiota, Y.; Yoshizawa, K.; Fujitsuka, M.; Shimakoshi, H. Effect of Macrocycles on the Photochemical and Electrochemical Properties of Cobalt-Dehydrocorrin Complex: Formation and Investigation of Co(I) Species. *Inorg. Chem.* **2023**, *62* (30), 11785-11795. DOI: 10.1021/acs.inorgchem.3c01718.
7. **Kametani, Y.**; Ikeda, K.; Yoshizawa, K.; Shiota, Y. Mechanistic Study of Reduction of Nitrite to NO by the Copper(II) Complex: Different Concerted Proton–Electron Transfer Reactivity between Nitrite and Nitro Complexes. *Inorg. Chem.* **2023**, *62*

(34), 13765-13774. DOI: 10.1021/acs.inorgchem.3c01854.

8. Nakamura, G.; Sakurai, M.; **Kametani, Y.**; Kawasaki, Y.; Shiota, Y.; Yoshizawa, K.; Ogo, S.; Matsumoto, T. Photosynthesis of NH_3 from NO_3^- Using CH_4 in Homogeneous Re Catalysis at Room Temperature and Normal Pressure. *ChemRxiv* **2024**. DOI: 10.26434/chemrxiv-2024-mzzcr-v2. This content is a preprint and has not been peer-reviewed.
9. Wakabayashi, T.; **Kametani, Y.**; Tanahashi, E.; Shiota, Y.; Yoshizawa, K.; Jung, J.; Saito, S. Ferrocenyl PNNP Ligands-Controlled Chromium Complex-Catalyzed Photocatalytic Reduction of CO_2 to Formic Acid. *J. Am. Chem. Soc.* **2024**, *146* (38), 25963-25975. DOI: 10.1021/jacs.4c03683.
10. Toyoshima, R.; **Kametani, Y.**; Yoshizawa, K.; Shiota, Y. The Effect of Intramolecular Proton Transfer on the Mechanism of NO Reduction to N_2O by a Copper Complex: A DFT Study. *Inorg. Chem.* **2024**, *63* (46), 22138-22148. DOI: 10.1021/acs.inorgchem.4c03619.
11. Nishimoto, K.; Noto, N.; **Kametani, Y.**; Grømer, B.; Murata, C.; Okuwa, H.; Shiota, Y.; Yoshizawa, K.; Saito, S. (PNCP)Ir vs. (PNNP)Ir: Neutral Iridium Complex for Direct Hydrogenation of Carboxylic Acids. *Organometallics* **2024**, *43* (23), 3013-3021. DOI: 10.1021/acs.organomet.4c00355.
12. Sääsk, V.; Abe, A.; **Kametani, Y.**; Shiota, Y.; Sato, O.; Adachi, C. Dynamic Luminescence Vapochromism of Pyridinium-Based Organic Salts. *Chem. Eur. J.* **2024**, *30* (69), e202402777. DOI: 10.1002/chem.202402777
13. **Kametani, Y.**; Shiota, Y. Mechanistic studies of NO_x reduction reactions involving copper complexes: encouragement of DFT calculations. *Dalton Trans.* **2024**, *53* (48), 19081-19087. DOI: 10.1039/D4DT02420F (*Frontier Article*)
14. Shichijo, K.; Tanaka, M.; **Kametani, Y.**; Shiota, Y.; Fujitsuka, M.; Shimakoshi, H. B_{12}-Catalyzed Carbonylation of Carbon Tetrahalides: Using a Broad Range of Visible Light to Access Diverse Carbonyl Compounds. *Chem. Eur. J.* **2024**, e202403663. DOI: 10.1002/chem.202403663.

List of Presentation at International Conferences

1) **Yohei Kametani**, Kei Ikeda, Yoshihito Shiota, Kazunari Yoshizawa “DFT study on nitrite reduction by copper complex: concerted asynchronous mechanism” *The 9th Tokyo Conference on Advanced Catalytic Science and Technology*, Fukuoka, Japan (July 26, 2022), Oral presentation.
2) **Yohei Kametani**, Tsukasa Abe, Yoshihito Shiota, Kazunari Yoshizawa “DFT Study on Mechanism of Nitric Oxide Reduction by Dicopper Complex” *10th Asian Biological Inorganic Chemistry Conference*, Kobe, Japan (November 29, 2022), Poster presentation.

Acknowledgements

The writing and completion of this dissertation would have never been possible without the assistance, support, and guidance of many teachers, colleagues, co-workers, and family members. It is my great pleasure to thank these people.

First of all, I would like to express my sincerest gratitude to my supervisor, Associate Professor Yoshihito Shiota, for teaching me about inorganic chemistry, theoretical chemistry, and providing detailed technical supports for computational chemistry. A lot of discussions with him were extremely meaningful and led to my personal growth. Without numerous discussions with him and his useful advice, I could not have completed this work.

I am deeply indebted to Professor Kazunari Yoshizawa for leading me to the fascinating research field of quantum chemistry and for teaching me the mindset and dedication required for research. His comments, suggestions, and encouragement have been of great value for my study.

I would like to acknowledge Professor Hisashi Shimakoshi for his invaluable insights and guidance throughout the review process of this dissertation. I am also grateful for the opportunity to engage with a diverse range of research topics in bioinorganic chemistry.

I am thankful to Associate Professor Yosuke Sumiya for his helpful advice and fruitful discussions. I am also thankful to Assistant Professor Tsukasa Abe, Dr. Masataka Yoshida, Taiji Nakamura, and Amit Shrestha, and Technical Staff Asuka Konomi for their kind comments on my research. I would like to thank all other members of the Yoshizawa laboratory and the Theoretical Chemistry laboratory for cultivating a supportive and inspiring research environment.

I am profoundly grateful to my friend, Dr. Keita Shichijo, for being a constant source of support and joy throughout these nine remarkable years of studying chemistry. I would also like to thank my partner, Rino Ogata, for her unwavering understanding and thoughtful support, which have helped me overcome many challenges.

Finally, I would like to dedicate this dissertation to my father, Tessho Kametani, with my deepest gratitude, and to my mother, Yumiko Kametani, and my little brother, Takehiro Kametani, for their continued support and warm encouragement.

Fukuoka, December 2024

Yohei Kametani